Ocean Engineering 264 (2022) 112506

Contents lists available at ScienceDirect

Ocean Engineering

journal homepage: www.elsevier.com/locate/oceaneng

Nonlinear noise of hydrofoil cavitation considering sound velocity variation and phase transitions

Lianjie Yu [a], Weiwen Zhao [a], Decheng Wan [a,*], Jianwei Wu [b]

[a] Computational Marine Hydrodynamic Lab (CMHL), School of Naval Architecture, Ocean and Civil Engineering, Shanghai Jiao Tong University, Shanghai, China
[b] Wuhan Second Ship Design and Research Institute, Wuhan, China

ARTICLE INFO

Keywords:
Cavitation noise
FW-H formulation
Direct volume integration
Wavy-leading-edge hydrofoil

ABSTRACT

Cavitation noise is an important part of underwater radiated noise (URN). It not only reduces the concealment and comfort of ships, but also affects marine life. In this paper, a detailed study of cavitation noise is carried out for NACA0012 hydrofoil and a wavy-leading-edge hydrofoil. The nonlinear sound pressure is computed by direct volume integration in FW-H formulation, considering the sound velocity change caused by the phase transition and the spherical sound source caused by the cavity volume change. By comparing with the experiment, the acoustic prediction method proposed in this paper is verified. The acoustic study is conducted from the perspectives of streamwise distribution, spanwise distribution, far-field directivity, influence of cavitation number and geometric influence. Three components and the sound source distributions are analyzed. The results show that, for cavitation state, nonlinear sound pressure is larger than the linear one and dominates in the near field. At further distances, the spherical component dominates. The cavitation noise of the modified hydrofoil is enhanced, and the source intensity is increased by 1–2 orders of magnitude.

1. Introduction

The noise research has become a hotspot recently. Underwater radiated noise (URN) not only affects the concealment and comfort of ships, but also has a negative impact on marine life. For this reason, the International Maritime Organization (IMO) formulated non-mandatory noise specifications for commercial ships (IMO, 2014). Cavitation noise is an important part of URN. It is difficult to predict and often related to violent phase transitions, multi-scale bubbles, turbulence and etc. Therefore, in-depth research on cavitation noise is needed urgently.

Direct numerical simulation (DNS) is the most accurate method to compute noise. However, the algorithms for the compressible fluid may not be suitable for hydroacoustics due to the conflict between the incompressible characteristics of the flow field and the compressibility of the sound field. To capture the sound accurately, the amount of grids is huge, which leads to a surge in the computation. Furthermore, DNS cannot compute the far-field sound pressure since only the result inside the domain is available. An alternative choice is acoustic analogy, whose basic idea is to decouple the flow field and sound field. The former is obtained by solving N–S equation with CFD, and the latter is integrated by Green's function, with the flow field data as inputting values. Acoustic analogy is first proposed by Lighthill (1952), who rewrote N–S equation into the wave motion form and obtained the Lighthill equation. After him, Curle (1955) obtained the Curle equation by the Kirchhoff integration, considering the existence of the solid wall. Based on them, Ffowcs Williams and Hawkings equation (FW–H equation) is derived (Ffowcs Williams and Hawkings, 1969), considering the object motion, which is the most commonly used formulation.

There are various expressions of FW-H equation, for example, Farrassat 1A equation (Farassat, 2007). In most of them, the quadrupole term (nonlinear term) is ignored. However, recent hydroacoustic studies have shown that the influence of nonlinear terms may be significant. More and more researchers pay attention to the nonlinear sources. The porous FW-H equation makes it possible to consider the nonlinear terms by selecting an integral surface in the fluid (Brentner, 1997). However, it is sensitive to the selection of the penetrable surface, and the end-cap problem occurs inevitably. The accurate way is the direct volume integration. Its biggest difficulty lies in the huge amount of grids for integration and different time delays for each grid, which is a challenge to the storage and calculation amount of the computer. Cianferra et al. (2019) proposed the MFP criterion. It is verified that the time delay effect can be ignored if the integration range satisfies the condition

* Corresponding author.
E-mail address: dcwan@sjtu.edu.cn (D. Wan).

https://doi.org/10.1016/j.oceaneng.2022.112506
Received 28 April 2022; Received in revised form 20 August 2022; Accepted 3 September 2022

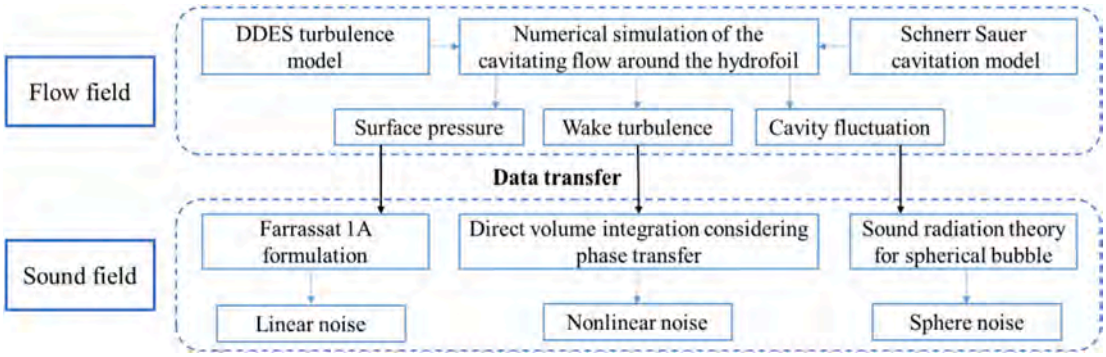

Fig. 1. The flow chart of the noise prediction method used in this paper.

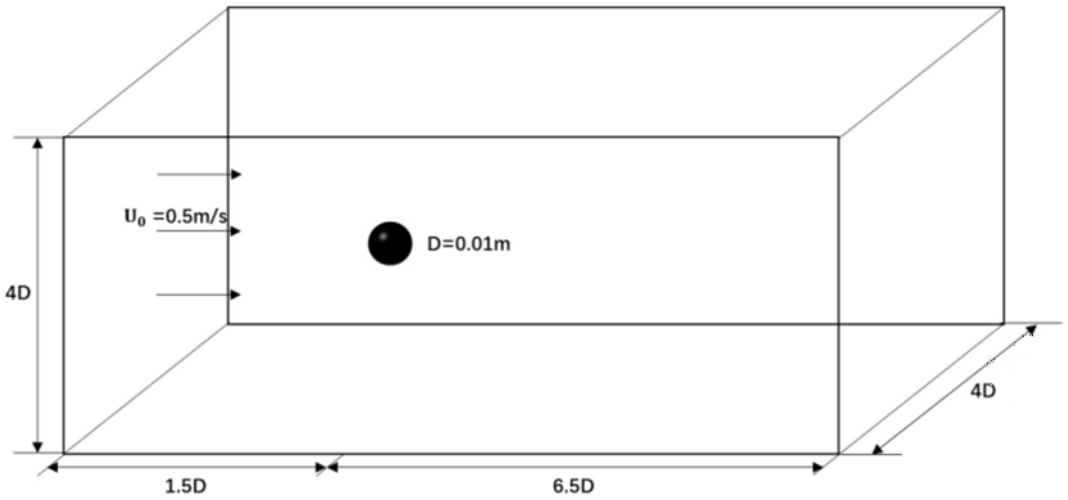

Fig. 2. The calculation domain for the flow around the sphere.

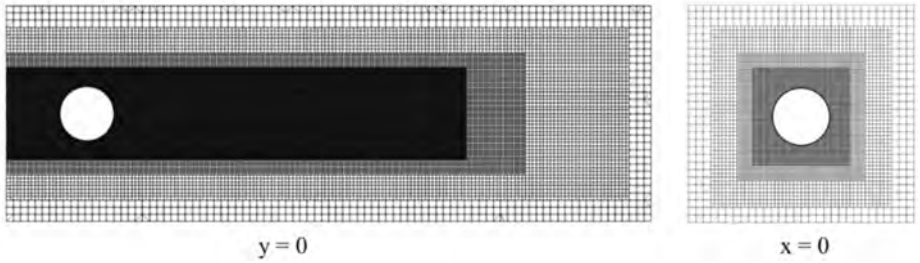

Fig. 3. The mesh shown in slices: The left panel is grid on the plane $y = 0$; The right panel is on the plane $x = 0$.

MFP > 1. This makes the direct volume integration practicable.

For the cavitation noise, in addition to the nonlinear term, another important sound source caused by phase transitions exists. Some previous papers ignored this part (Kim et al., 2018). However, in recent years, studies have shown that the sound source caused by the phase transition has a great impact on the cavitation noise (Ianniello et al., 2013, 2014). Generally, such sound is computed by the spherical wave radiation law (Wu et al., 2018; Wei et al., 2022). The advantage is that the pulsation caused by the cavity volume change can be considered. The disadvantage is that it ignores the sound source induced by the bubble deformation and the cavity collapse. In fact, unless high-precision simulation, like DNS, is used, the phenomenon of cavitation collapse is difficult to capture in CFD.

The hydrofoil is regarded as a simplified model of the propeller and often used to investigate the mechanisms of cavitation. If the cavity length does not exceed half of the chord, it is generally considered to be sheet cavitation (steady cavitation). Unstable pressure fluctuations exist in the closure region, resulting in violent noise (Ahn et al., 2016). A number of experiments and numerical simulations focus on hydrofoil sheet cavitation noise, including baseline hydrofoils and modified ones (Li et al., 2020; Pendar et al., 2021). However, there are few researches on the nonlinear sound pressure for the hydrofoil cavitation, especially with the direct volume integration. In this paper, the nonlinear noise is studied in detail for NACA0012 hydrofoil and a modified wavy-leading-edge hydrofoil. The noise component caused by phase transition is computed with volume integration as well.

An accurate simulation of cavitation is the basis of cavitation noise prediction. Some researchers compared the differences in cavitation noise predicted by different turbulence models (Moghadam et al., 2016). It is found that RANS is inaccurate to predict noise because it ignores the pulsations of the quantities (Ianniello et al., 2013). LES needs a huge amount of grids and calculations, making it not suitable for engineering

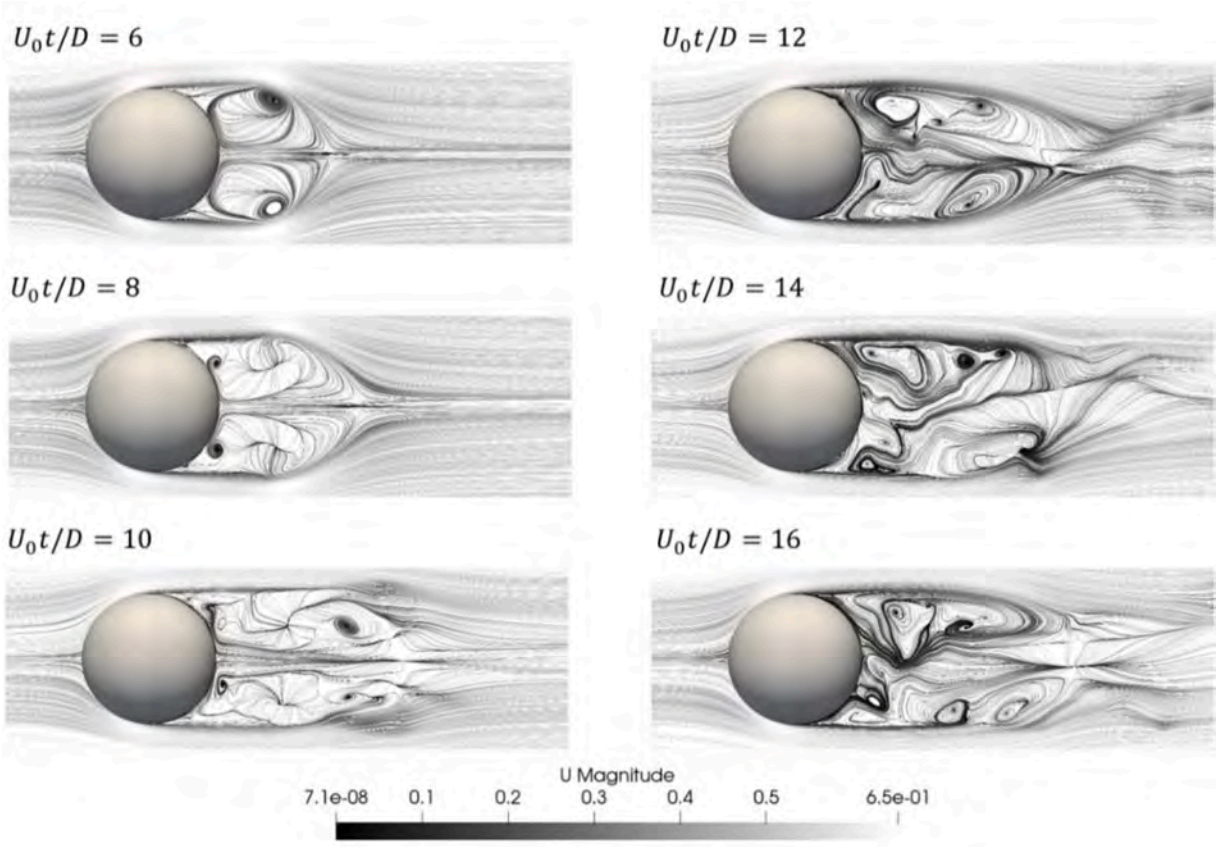

Fig. 4. The snapshots for the streamlines at the top view: The pair of large vortex is obvious at $U_0t/D = 6$; The vortex range of 2D is obvious at $U_0t/D = 10$; The small vortex is obvious at $U_0t/D = 12$, 14 **and** 16.

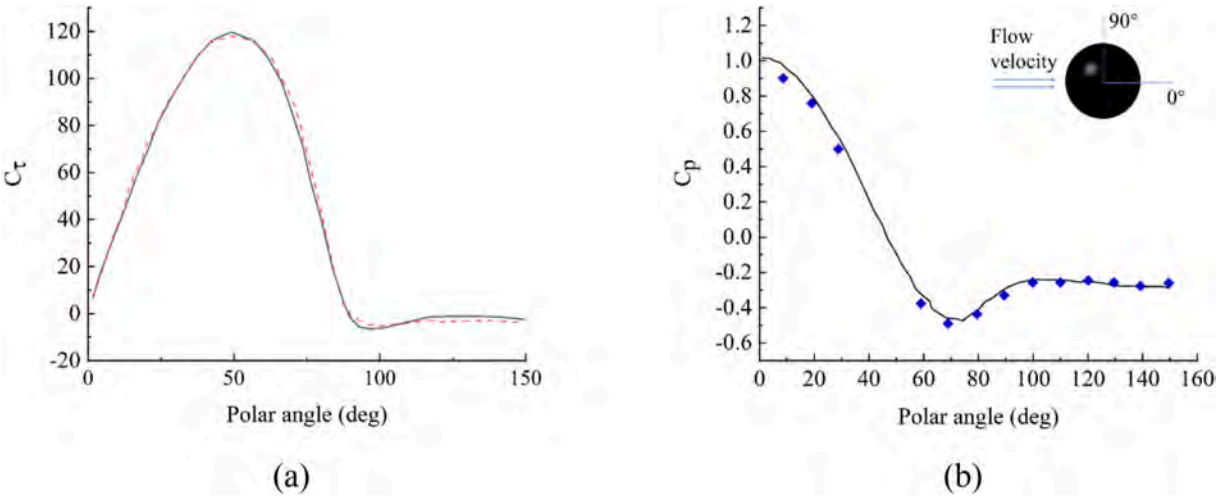

Fig. 5. The force coefficients expressed in polar angles: (a) The skin friction coefficient along the circumferential direction is the grey solid line; the DNS result (Seidl et al., 1997) is the red dash line. (b) The pressure coefficient along circumferential direction is the black solid line; the experiment result (Kim and Durbin, 1988) is the blue scatter. (For interpretation of the references to color in this figure legend, the reader is referred to the Web version of this article.)

cavitation problems (Li et al., 2020). DES turbulence model is used in cavitation noise forecast the most widely (Greschner et al., 2008; Seo and Lele, 2009). The phase transition is considered by the mass transport model (cavitation model). Commonly-used cavitation models include Merkle model (Merkle et al., 1998), Schnerr-Sauer model (Schnerr and Sauer, 2001), Zwart-Gerber-Belamri model (Zwart et al., 2004) and so on. In this paper, the most widely-used Schnerr Sauer cavitation model is adopted, combined with DES turbulence model.

The innovation of this paper is that the direct volume integration is used to calculate the cavitation noise, and a new method that considers the sound velocity change caused by the phase transition is proposed. The distribution law of linear term, nonlinear term and sphere sound pressure is studied systematically, and the effects of cavitation number and wavy leading edge on cavitation noise are discussed.

The structure of this paper is arranged as follows. Section 2 introduces the mathematical formulations, including the form of the

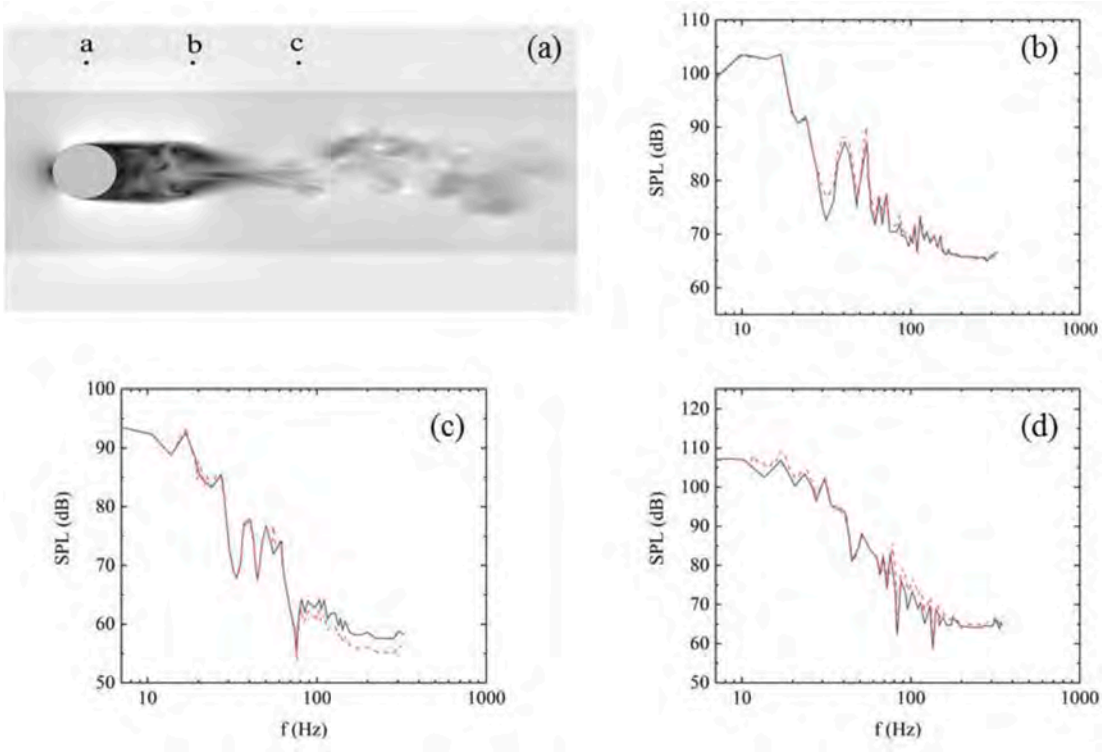

Fig. 6. (a) The volume integration region and the position of near-field probes 'a', 'b' and 'c'. (b)–(d) is the SPL at microphone 'a' – 'c' respectively. The black solid line represents the prediction in this paper; the red dash line represents the literature values (Cianferra et al., 2018). (For interpretation of the references to color in this figure legend, the reader is referred to the Web version of this article.)

quadrupole volume integration in FW-H equation, the sphere source due to phase transitions, the Schnerr Sauer cavitation model and DDES turbulence model. Section 3 presents the acoustic results causing by the flow around a sphere. This case is to validate the accuracy of the volume integration. Section 4 gives the numerical setup for NACA0012 hydrofoil cavitation and comparison with experiments in hydrodynamics and hydroacoustics. In Section 5, the cavitation noise is analyzed in detail, including streamwise and spanwise acoustic characteristics for different noise components, far-field directivity, the effect of cavitation number on nonlinear components and source distributions, and the effect of wavy-leading-edge. Relevant discussions and important conclusions are given in Section 6.

2. Mathematical foundation

2.1. Turbulence model

The interaction between turbulence and cavitation is particularly complex. Previous studies proved that RANS model cannot obtain the small-scale vortices in the cavitation flow, which has a great impact on the acoustic prediction.

For this reason, this paper adopts the improved Spalart-Allmaras DES as the turbulence model, namely SA-DDES (Spalart and Allmaras, 1992). Its governing equation is

$$\frac{\partial\widetilde{\nu}}{\partial t}+div(\widetilde{\nu}u)=\frac{1}{C_\sigma}\left\{div[(\nu+\widetilde{\nu})grad\widetilde{\nu}]+C_{b2}\frac{\partial\widetilde{\nu}}{\partial x_i}\frac{\partial\widetilde{\nu}}{\partial x_j}\right\}+C_{b1}\widetilde{S}\widetilde{\nu}-C_{w1}f_w\left(\frac{\widetilde{\nu}}{\widetilde{d}}\right)^2 \tag{1}$$

The transient and term is on the left side; The right side is the diffusion term, source term, and the dissipation term respectively. The DDES equation modifies $\widetilde{d}$ in the formula to

$$\widetilde{d}=d_w-f_d\cdot\max(d_w-C_{DES}\Delta,0) \tag{2}$$

$$f_d=1-\tanh\left[(8r_d)^3\right] \tag{3}$$

$$r_d=\frac{\nu_t+\nu}{\sqrt{U_{ij}U_{ij}}(\kappa d_w)^2} \tag{4}$$

2.2. Cavitation model

The cavitation model is derived from Rayleigh-Plesset cavity dynamics equation. The phase changes caused by condensation and evaporation are described by adding source terms. There are various mass transport models, among which, Schnerr-Sauer cavitation model is adopted in this paper. The model equation is as follows (Schnerr and Sauer, 2001):

$$\frac{\partial(\rho_v\alpha_v)}{\partial t}+\frac{\partial(\rho_v\alpha_v u_j)}{\partial x_j}=\dot{m}^+-\dot{m}^- \tag{5}$$

The source terms $\dot{m}^+$ and $\dot{m}^-$ represent the evaporation and condensation processes, respectively. When the phase transition occurs, there is

$$\dot{m}^+=\frac{\rho_v\rho_l}{\rho}\alpha_v(1-\alpha_v)\frac{3}{R_b}\sqrt{\frac{2}{3}\frac{\max(p_v-p,0)}{\rho_l}} \tag{6}$$

$$\dot{m}^-=\frac{\rho_v\rho_l}{\rho}\alpha_v(1-\alpha_v)\frac{3}{R_b}\sqrt{\frac{2}{3}\frac{\max(p-p_v,0)}{\rho_l}} \tag{7}$$

Among them, R_b represents the cavity radius, and p_v is the saturation vapor pressure at the local temperature. The calculation formula of the cavity radius is:

$$\mathrm{R_b}=\left(\frac{\alpha_v}{(1-\alpha_v)}\frac{3}{4\pi}\frac{1}{N_b}\right)^{\frac{1}{3}} \tag{8}$$

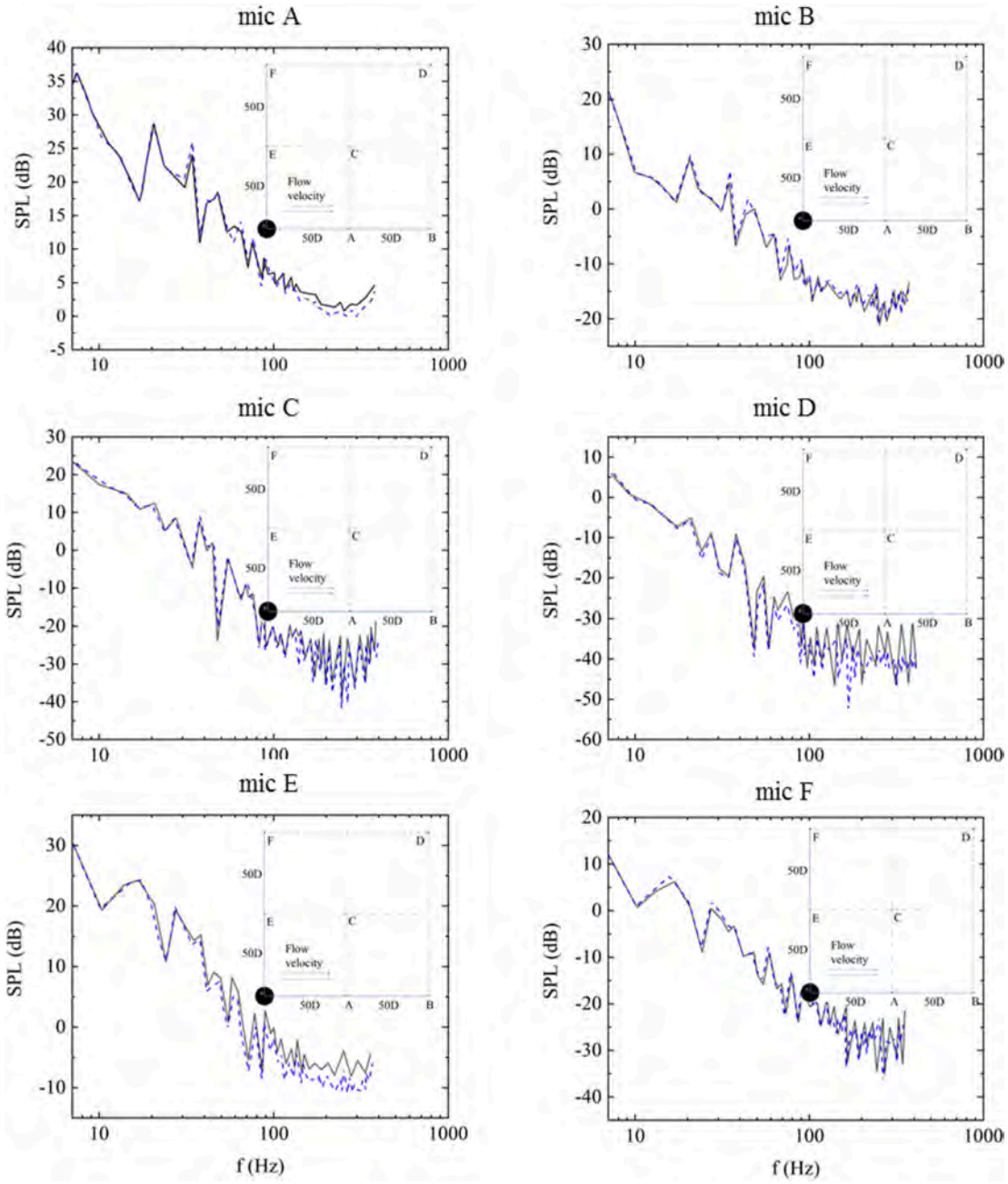

Fig. 7. The diagram of six far-field microphones. The black solid line represents the prediction in this paper; the blue dash line represents the literature results. The scale is not actual for viewing convenience. (For interpretation of the references to color in this figure legend, the reader is referred to the Web version of this article.)

where $N_b = 10^{13}\ m^{-3}$ is the cavity number density.

2.3. Quadrupole volume integration

Ffowcs Williams and Hawkings (1969) deduced the so-called FW-H equation. It is transformed from the Navier-Stokes equation. The left side of the formulation is in a wave equation form, and the right side is three types of source terms, as the formula shows.

$$\boxdot^2 p' = \frac{\partial}{\partial t}[\rho_0 v_n \delta(f)] - \frac{\partial}{\partial x_i}[p n_i \delta(f)] + \frac{\partial^2}{\partial x_i \partial x_j}[H(f) T_{ij}] \tag{9}$$

where $\boxdot^2 = \frac{1}{c^2}\frac{\partial^2}{\partial t^2} - \nabla^2$ is the wave operator or D'Alembertian operator. c and ρ_0 represent the speed of sound and undisturbed density respectively. v_n represents the normal velocity at the local element. p represents the gage pressure on the object surface. $T_{ij} = \rho u_i u_j - \sigma_{ij} + (p' - c^2\rho')\delta_{ij}$ is called Lighthill stress tensor. σ_{ij} is the viscous stress tensor and δ_{ij} is the Kronecker delta. $H(f)$ and $\delta(f)$ represent the Heaviside and Dirac delta functions respectively.

The first two terms on the right side of formula (1) represent monopole and dipole respectively. To solve them, the surface integration is needed. The third term needs the volume integration.

To obtain the solution, Green's function is used to integrate. Without loss of generality, it is assumed that the incoming flow is along the x_1

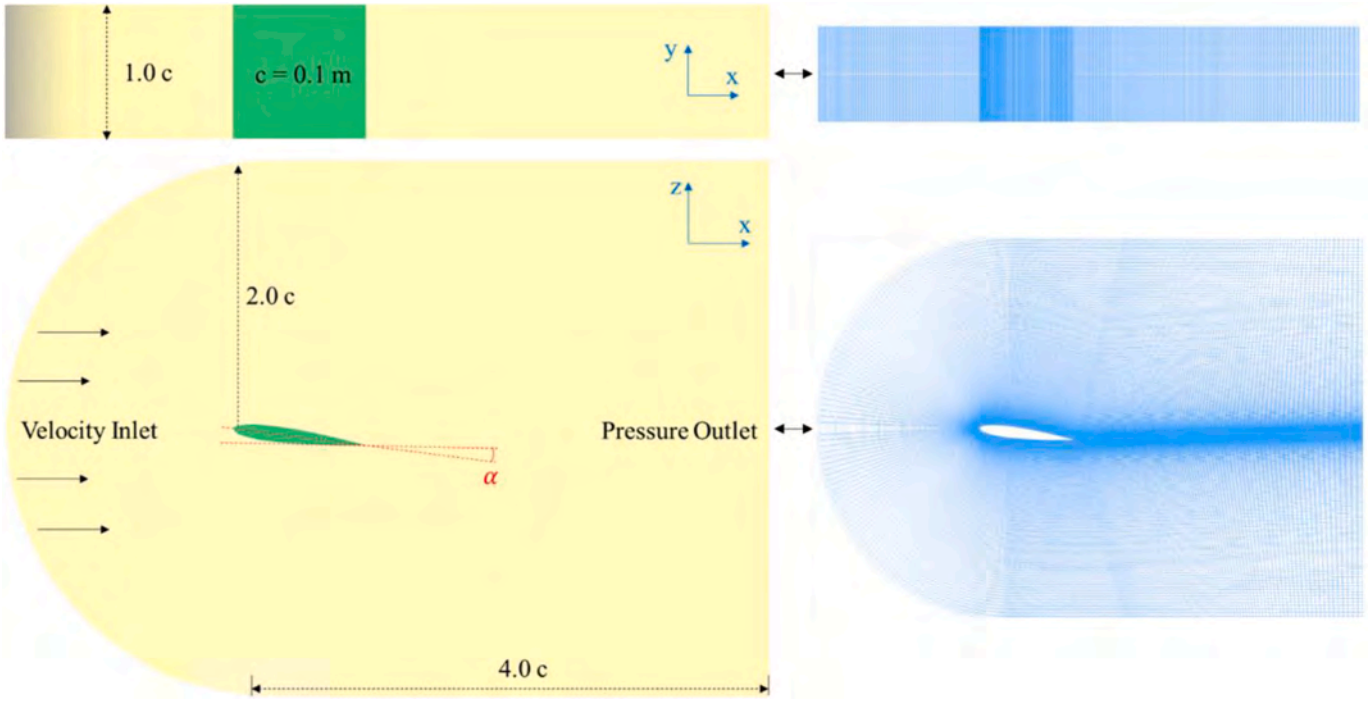

Fig. 8. The domain and grids for hydrofoil: The top view and side view are presented, with mesh in blue color. (For interpretation of the references to color in this figure legend, the reader is referred to the Web version of this article.)

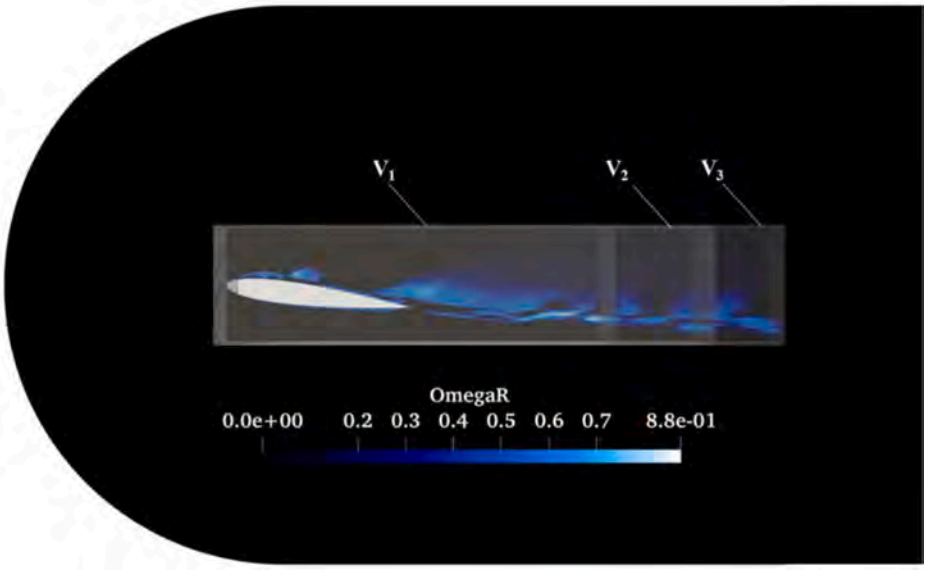

Fig. 9. Three volume integration ranges for nonlinear acoustic computation. The color map is rendered by $\boldsymbol{\Omega_R}$. (For interpretation of the references to color in this figure legend, the reader is referred to the Web version of this article.)

direction. Green's function in convective form is $G(\mathbf{x},t;\mathbf{y},\tau) = \frac{\delta(g)}{4\pi r^*}$. To obtain the two-order spatial derivative of Green's function, more attention is paid to $\frac{\partial^2}{\partial x_i \partial x_j}\left[\frac{\delta(g)}{r^*}\right]$. The derivative formula of the quotient is used, combined with the chain derivative rule. Considering $t = \tau + \frac{r}{c_0}$, the final expression is obtained (see Cianferra et al. (2019) for details):

$$\frac{\partial^2}{\partial x_i \partial x_j}\left[\frac{\delta(g)}{r^*}\right] = \frac{1}{c_0}\left[\frac{2\widehat{r}_i\widehat{r}_j^*}{r^{*2}} + \frac{1}{\beta^2 r^{*2}}\left(\widehat{r}_i^*\widehat{r}_j^* - R_{ij}^*\right)\right] + \frac{1}{c_0^2}\frac{\widehat{r}_i\widehat{r}_j}{r^*}\frac{\partial^2}{\partial t^2}[\delta(g)] + + \left[\frac{3\widehat{r}_i^*\widehat{r}_j^* - R_{ij}^*}{r^{*3}}\right]\delta(g) \tag{10}$$

where $R_{ij}^* = \begin{bmatrix} 1 & 0 & 0 \\ 0 & \beta^2 & 0 \\ 0 & 0 & \beta^2 \end{bmatrix}$.

When $M_0 \ll 1$, we have $\beta \approx 1$, and consequently $r = r^*$, $R_{ij}^* = \delta_{ij}$. At this time, equation (10) can be simplified as:

$$\frac{\partial^2}{\partial x_i \partial x_j}\left[\frac{\delta(g)}{r}\right] = + \frac{1}{c_0^2}\frac{\widehat{r}_i\widehat{r}_j}{r}\frac{\partial^2}{\partial t^2}[\delta(g)] + \frac{1}{c_0}\left[\frac{3\widehat{r}_i\widehat{r}_j - \delta_{ij}}{r^2}\right]\frac{\partial}{\partial t}[\delta(g)] + \left[\frac{3\widehat{r}_i\widehat{r}_j - \delta_{ij}}{r^3}\right]\delta(g) \tag{11}$$

Finally, the form of the quadrupole volume integration is obtained:

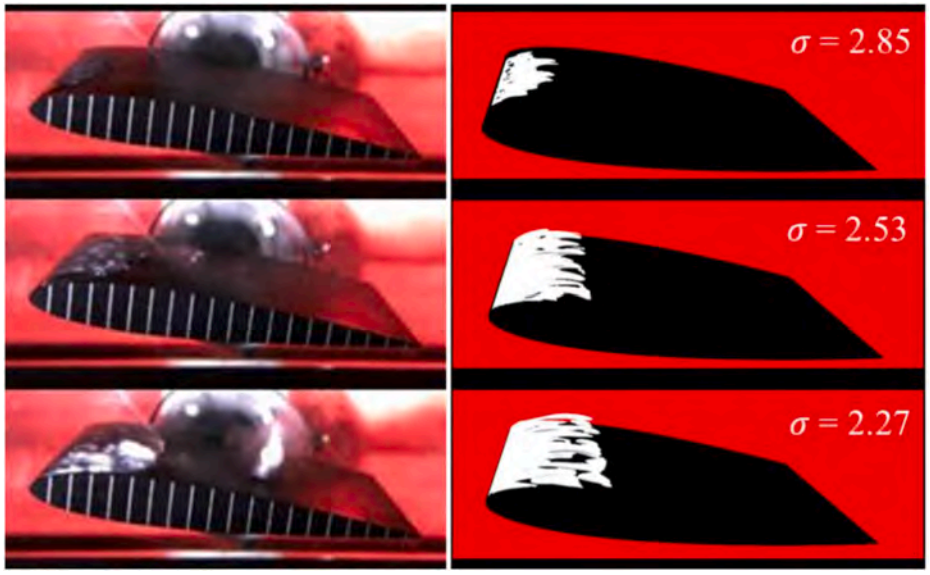

Fig. 10. The experiment results (the left column) and the simulated cavity state (the right column).

Table 1
Comparison of simulated cavitation length with experimental results under different cavitation number.

Cavitaion number α	Cavity length (m, EFD)	Cavity length (m, CFD)	Difference (%, CFD-EFD)
2.85	0.0100	0.0104	4.0
2.53	0.0190	0.0197	3.7
2.27	0.0300	0.0309	3.0

$$4\pi\widehat{P}_{3D}(x,t)=\frac{1}{c_0^2}\frac{\partial^2}{\partial t^2}\int_{f>0}\left\{T_{ij}\left[\frac{\widehat{r}_i\widehat{r}_j}{r^*}\right]\right\}_\tau dV+\frac{1}{c_0}\frac{\partial}{\partial t}\int_{f>0}\left\{T_{ij}\left[\frac{2\widehat{r}_r\widehat{r}_j^*}{r^*}+\frac{\widehat{r}_i^*\widehat{r}_j^*-R_{ij}^*}{\beta^2 r^{*2}}\right]\right\}_\tau dV+\int_{f>0}\left\{T_{ij}\left[\frac{3\widehat{r}_i^*\widehat{r}_j^*-R_{ij}^*}{r^{*3}}\right]\right\}dV \tag{12}$$

2.4. Cavity sphere noise

In this paper, the source of the cavity noise is regarded as the time-domain pulsating sphere (Wu et al., 2018; Wei et al., 2022). The radiated sound pressure generated by the cavity volume change can be expressed as:

$$p'_{cav}(\boldsymbol{x},t)=\frac{\dot{Q}(t-\boldsymbol{x}/c_0)}{4\pi r} \tag{13}$$

$$Q\equiv\int qdV=\frac{d}{dt}(\rho V) \tag{14}$$

Here, p'_{cav} represents the sound pressure caused by the cavitation. q is the mass pulsation per unit volume. V is the cavity volume, and $\boldsymbol{x}$ is the distance vector from the element to the microphone. The superscript $\cdot$ represents time derivative. Besides, there is no need to consider the time delay effect once ignore the compressibility.

The vapor volume fraction is used to represent the contribution of cavitation noise, as follows:

$$p'_{cav}(\boldsymbol{x},t)=\frac{\rho_0}{4\pi}\frac{\partial}{\partial t}\left[\frac{1}{r}\int_V\frac{\partial\alpha_V}{\partial t}dV\right] \tag{15}$$

where α_V represents the vapor volume fraction.

When applying the volume integration in Section 2.3 to the cavitating flow, the changes in density and sound velocity need to be considered (determined by the medium of vapor or water). In this paper, the linear interpolation is used mainly:

$$\rho_{cav}=\alpha_V\rho_V+(1-\alpha_V)\rho_W \tag{16}$$

$$c_{cav}=\alpha_V c_V+(1-\alpha_V)c_W \tag{17}$$

where ρ_{cav} and c_{cav} is the density and speed of sound for cavitating flow. $\rho_V=0.02308$ kg/m^3 and $\rho_W=1000$ kg/m^3 are density for pure vapor and water medium. Similarly $c_V=340$ m/s and $c_W=1400$ m/s.

The linear term is obtained by the integration of the dipole on the object surface in Farrassat 1A equation, and its corresponding physical meaning is the sound source caused by the pressure fluctuation on the hydrofoil surface. The nonlinear noise is computed from the direct volume integration of the quadrupole in the Lighthill equation, and its corresponding physical meaning is the sound source caused by the turbulent fluctuation such as the wake and vortex shedding. Sphere noise is a monopole sound source, and its corresponding physical meaning is the sound caused by density changes and cavity pulsation. The three components are calculated separately. The schematic diagram of the acoustic prediction in this paper is shown as Fig. 1.

3. Validation of the volume integration

To verify the acoustic volume integration, the single-phase flow around a sphere is simulated in this chapter and compared with the literature (Cianferra et al., 2018). All computations in this paper are performed on OpenFOAM platform. The chapter is divided into three parts. The first part introduces the numerical settings. The hydrodynamic results are shown in the second part, laying the foundation for the acoustic prediction. The acoustic validation is performed in the third part.

3.1. Numerical setup

Following the settings of (Cianferra et al., 2018), the sphere diameter is set as 0.01m. The domain is a rectangle of 12D × 4D × 4D, and the inflow velocity is 0.5 m/s. Therefore, the Reynolds number $Re_D=5000$ is based on the diameter. The sphere is located in the center of the domain, 1.5D from the inlet and 6.5D from the outlet, as Fig. 2 shows.

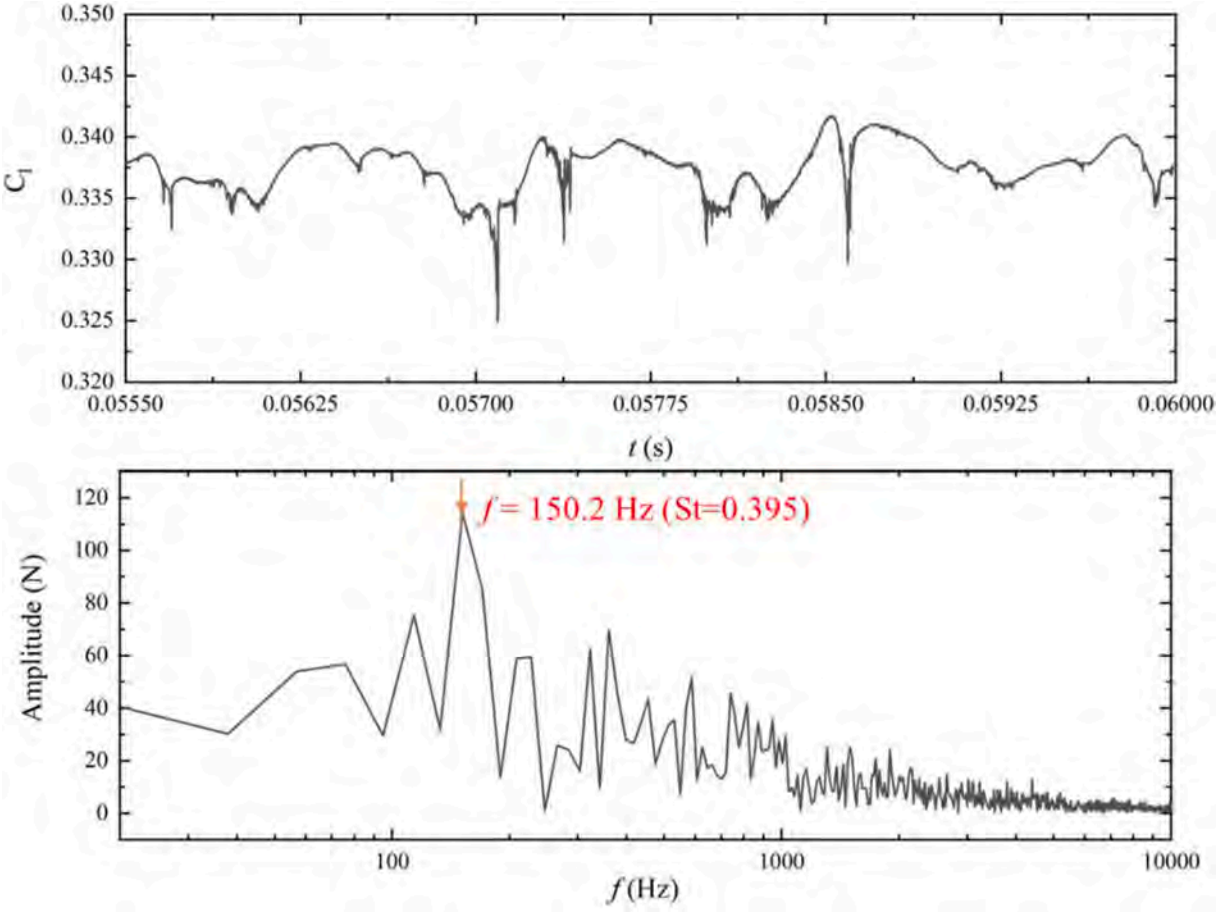

Fig. 11. The time history of lift coefficient (the top panel) and the frequency history (the bottom panel), with $\mathbf{C_l} = \frac{F_l}{\frac{1}{2}\rho V_\infty{}^2 S_L}$; The Strouhal number is $\mathbf{St} = \frac{fl}{V_\infty}$.

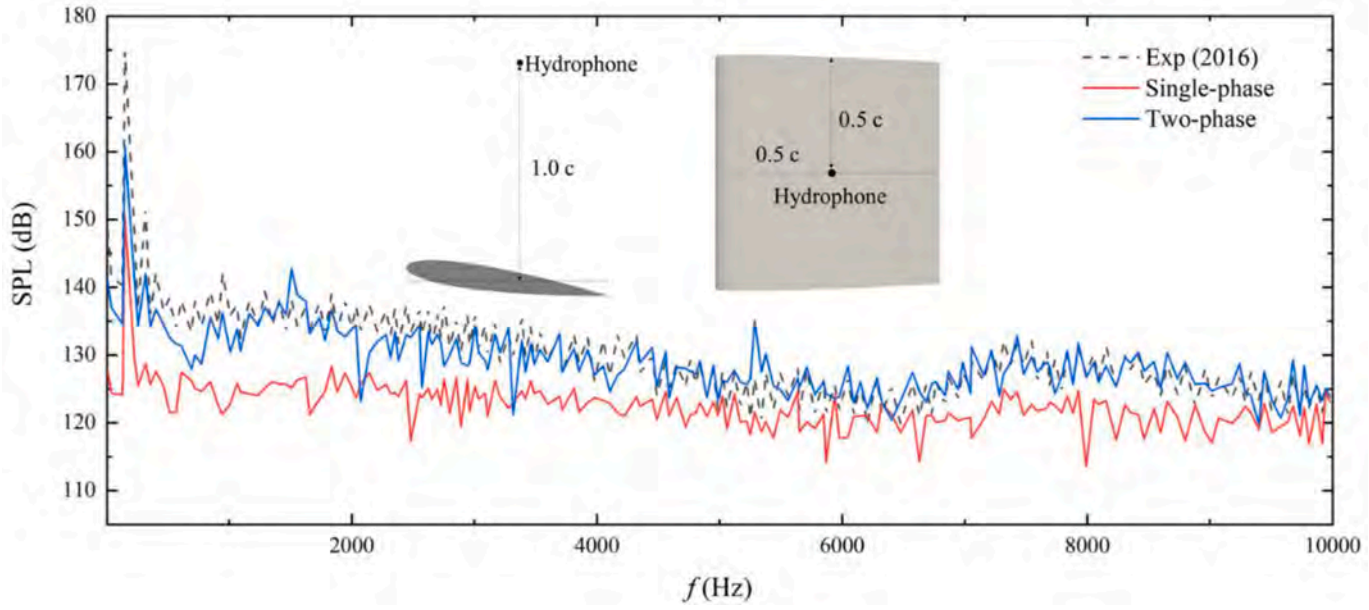

Fig. 12. $\sigma = 2.85$ working condition: The dotted line represents the experiment results, the red line represents the prediction of the sound pressure without considering the change of the two-phase sound speed, and the blue line represents the prediction result considering the sound speed change. (For interpretation of the references to color in this figure legend, the reader is referred to the Web version of this article.)

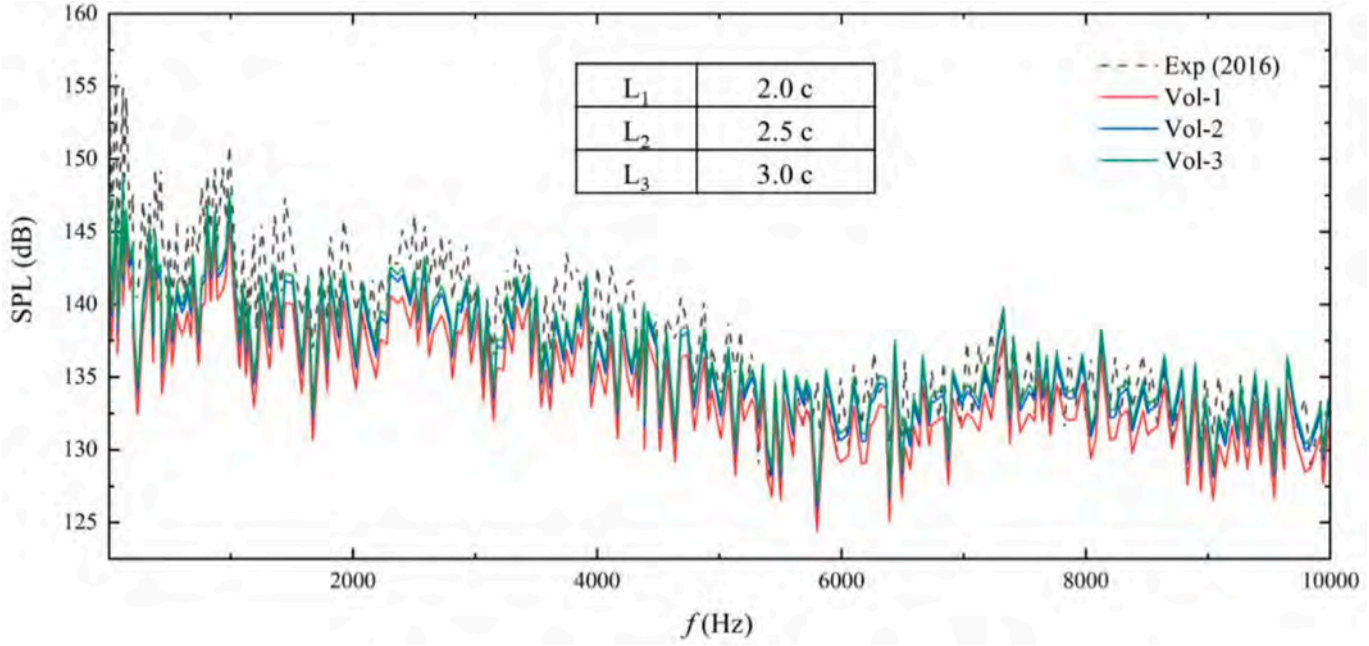

Fig. 13. $\sigma = 2.53$ working condition: Three integration ranges have the same size in the x and y directions, and the lengths in the x direction are $L_1 = 2c$, $L_2 = 2.5c$, $L_3 = 3c$ respectively, represented by three colors of red, blue and green. (For interpretation of the references to color in this figure legend, the reader is referred to the Web version of this article.)

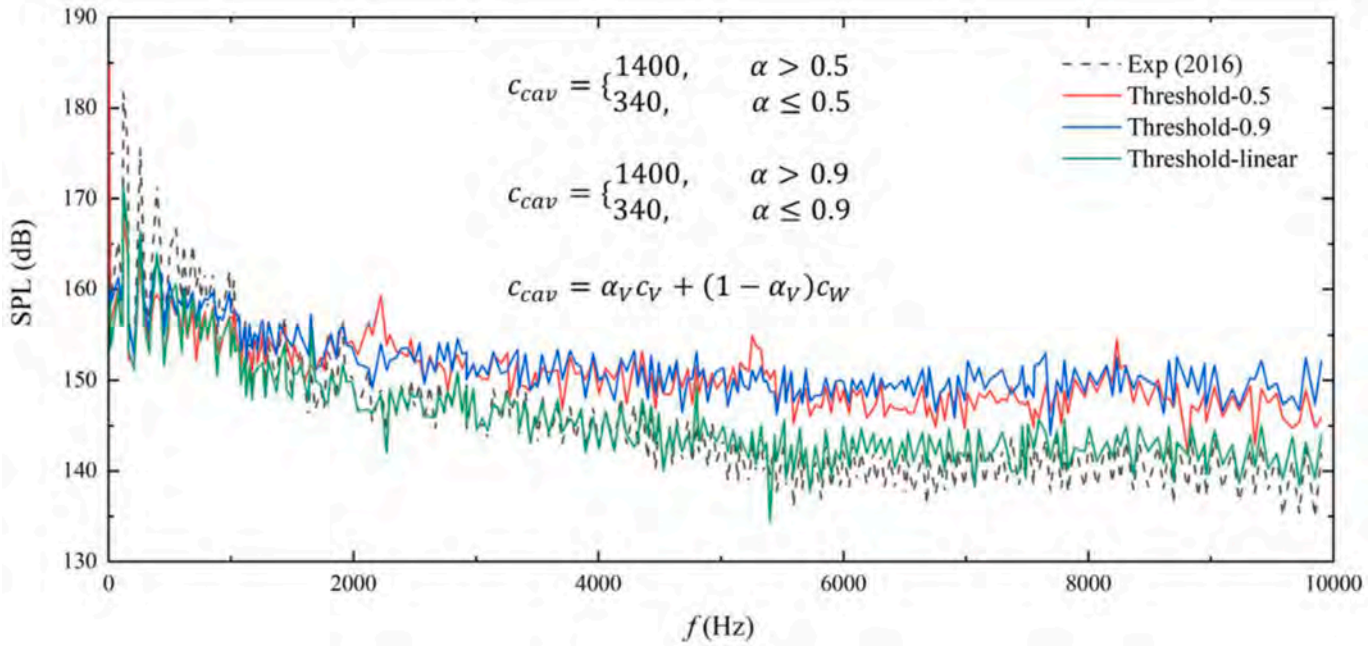

Fig. 14. $\sigma = 2.27$ working condition: The sound speed in two-phase is represented by c_{cav}. The value of water sound speed is $c_W = 1400 m/s$, and that in vapor is $c_V = 340 m/s$.

An unstructured grid is used near the sphere, and a structured mesh is applied in the area away from the object. As is shown in Fig. 3, three refinement levels are set in the computational domain, and 10 thin elements are set near the sphere as the boundary layer. The minimum value of y+ is about 0.8.

3.2. Hydrodynamic results

As a bluff body, vortex shedding for the sphere is obvious. Therefore, the volume integration is important for this case. The snapshots of the streamlines are shown in Fig. 4. The separation point of the sphere is about 90°. The large vortices pairs move over time, and separate out the small vortices downstream. The small vortices move downstream and dissipate gradually. The range of the vortex is about 2D, which is consistent with the literature (Cianferra et al., 2018).

Fig. 5 shows the force coefficients along the circumferential direction varying with the polar angle. The formula of the skin friction coefficient and the pressure coefficient are written as $C_\tau = \tau_w \mathrm{Re}/\rho_0 U_0^2$, $C_p = (p - p_0)/0.5\rho_0 U_0^2$. The former is compared with the DNS results (Seidl et al., 1997), showing good consistency. The pressure coefficient is compared

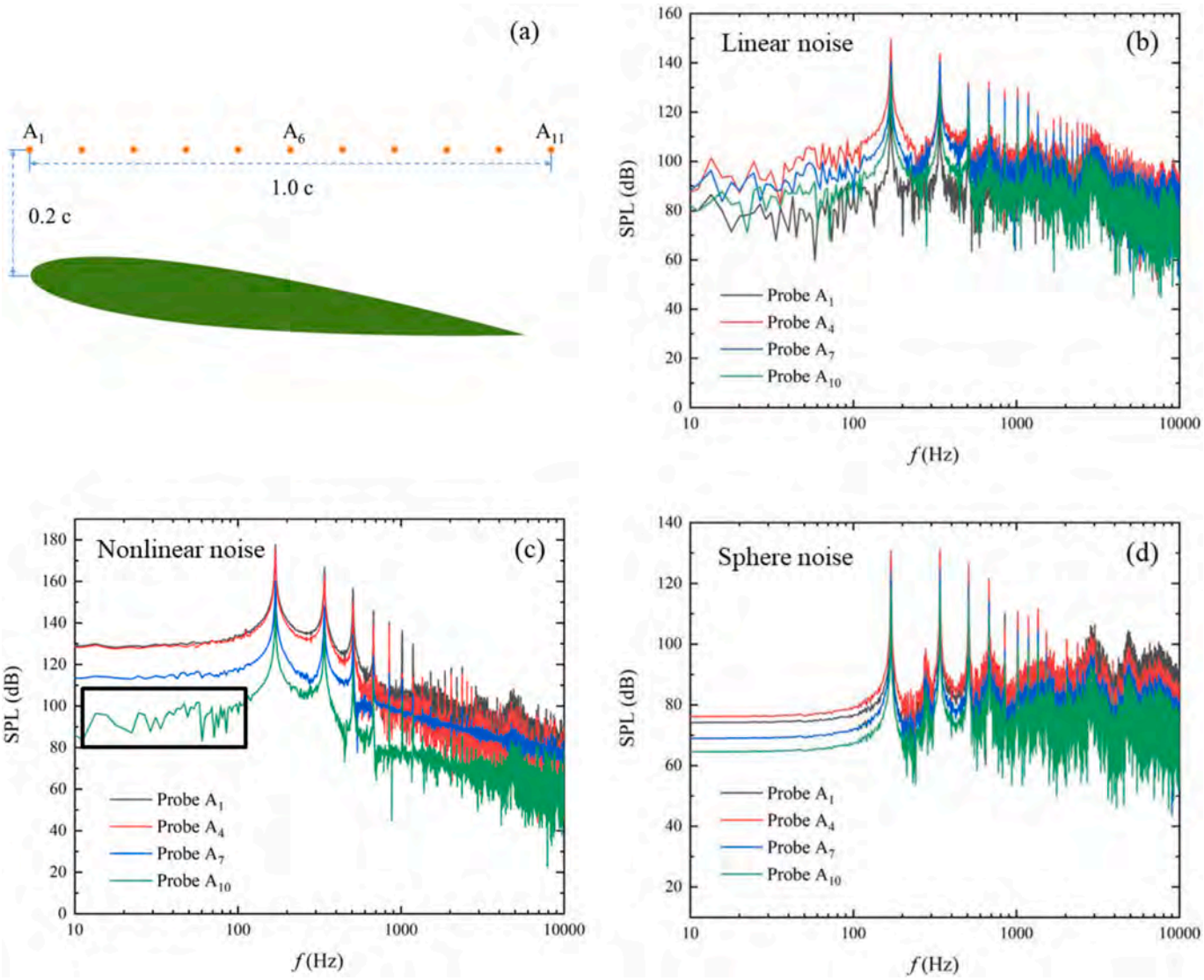

Fig. 15. (a) Sketch of streamwise microphone positions; (b) (c) (d): The linear noise, nonlinear noise and sphere noise predicted at A_1, A_4, A_7 and A_{10} probes.

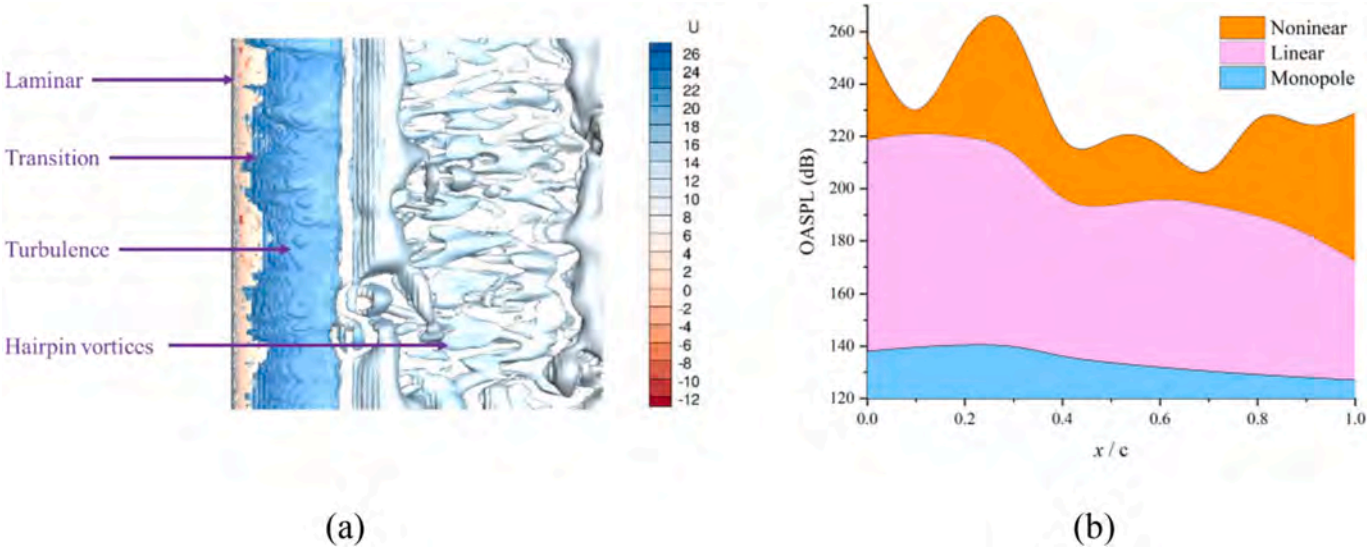

Fig. 16. (a) The development of the turbulence for cavitation; (b) OASPL calculated for different components at 11 probes (A_1 - A_{11}).

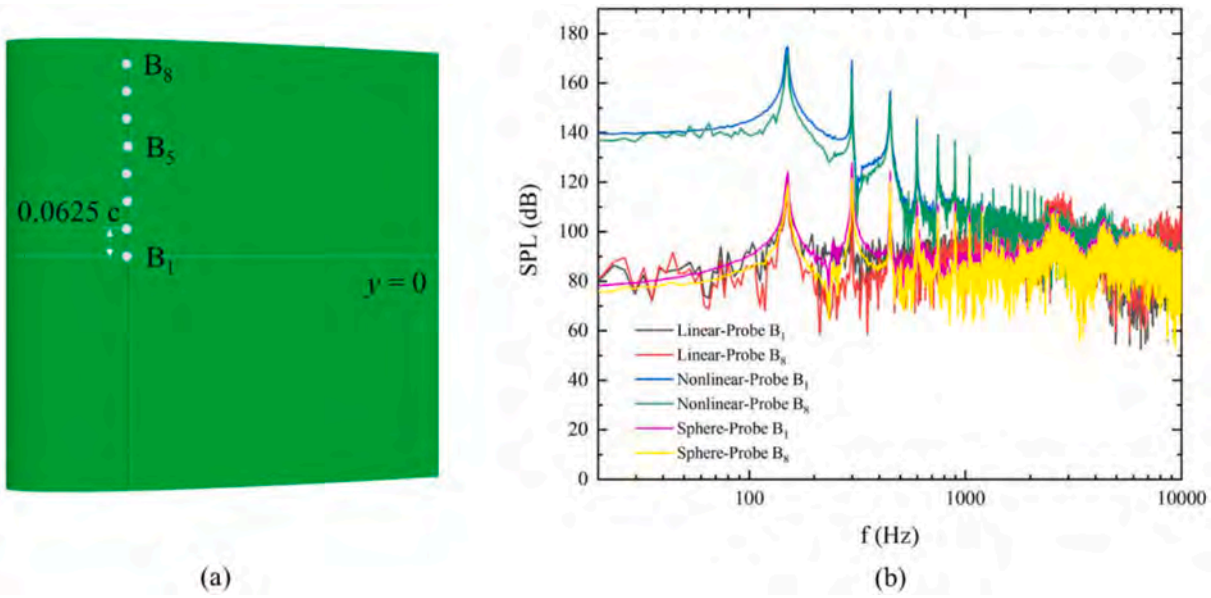

Fig. 17. (a) The sketch of microphones' positions in spanwise direction; (b) The linear, nonlinear and sphere noise predicted at B_1 and B_8 probes.

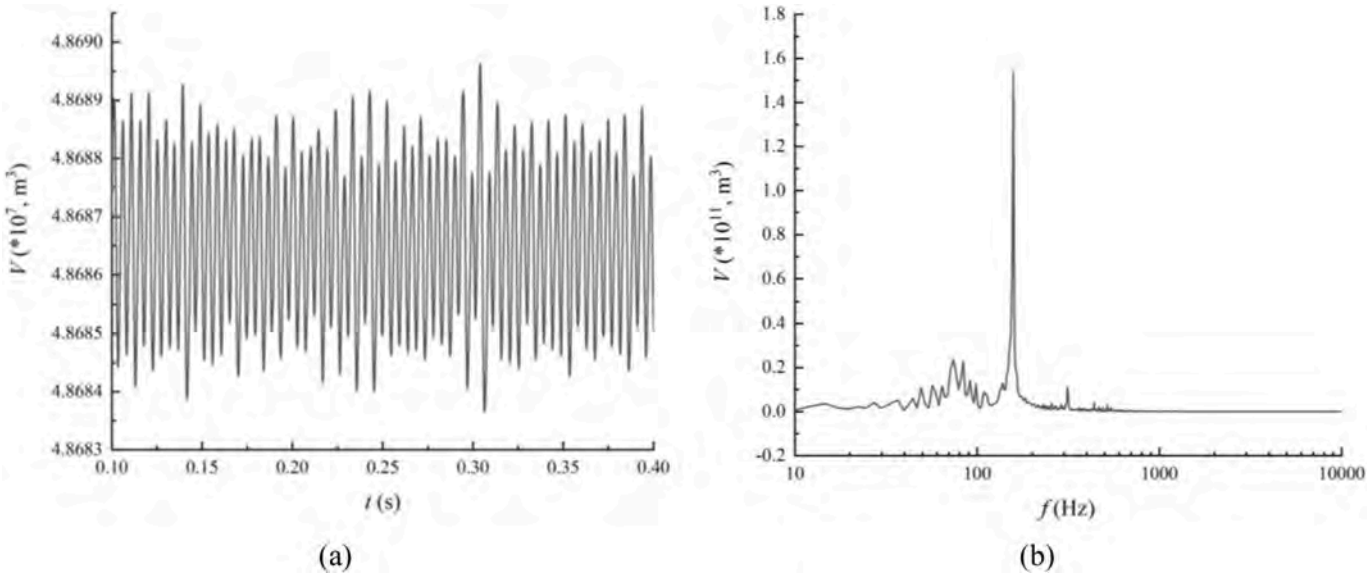

Fig. 18. (a) The time history of cavity volume for $\boldsymbol{\sigma} = 2.27$; (b) The frequency history of cavity volume.

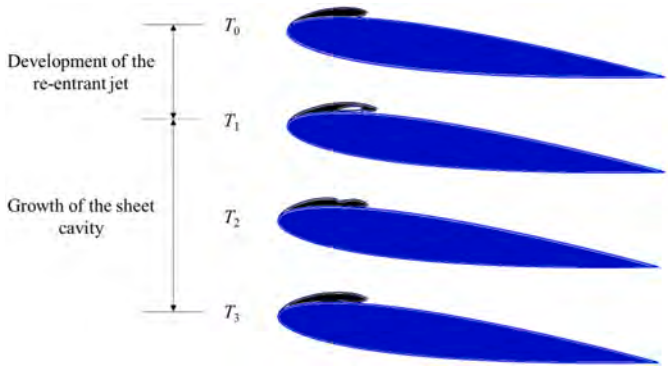

Fig. 19. Four typical stages for sheet cavitation in a cycle.

with the experiment (Kim and Durbin, 1988), which is in good agreement and reproduces the experimental separation angle ($\theta \approx 70°$).

3.3. Acoustic results

The acoustic predictions are verified using the formula mentioned in section 2.3. The region of the volume integration is consistent with the literature (Cianferra et al., 2018), as shown in Fig. 6(a). This region covers almost all turbulent effects (including vortex shed, recirculation, etc.). Therefore, all quadrupoles are covered.

Three near-field sound pressure probes 'a', 'b', 'c' are selected, whose coordinates are (0, 2D, 0), (2D, 2D, 0), (4D, 2D, 0). The sound pressure is described by sound pressure level (SPL). $\mathrm{SPL} = 20{*}\log_{10}(p/p_{ref})$, where $p_{ref} = 1 \times 10^{-6}$Pa is the reference pressure. The acoustic results are the sum of linear terms (integration on the object surface) and nonlinear terms (integration on the volume region). Good consistency is shown comparing with the literature.

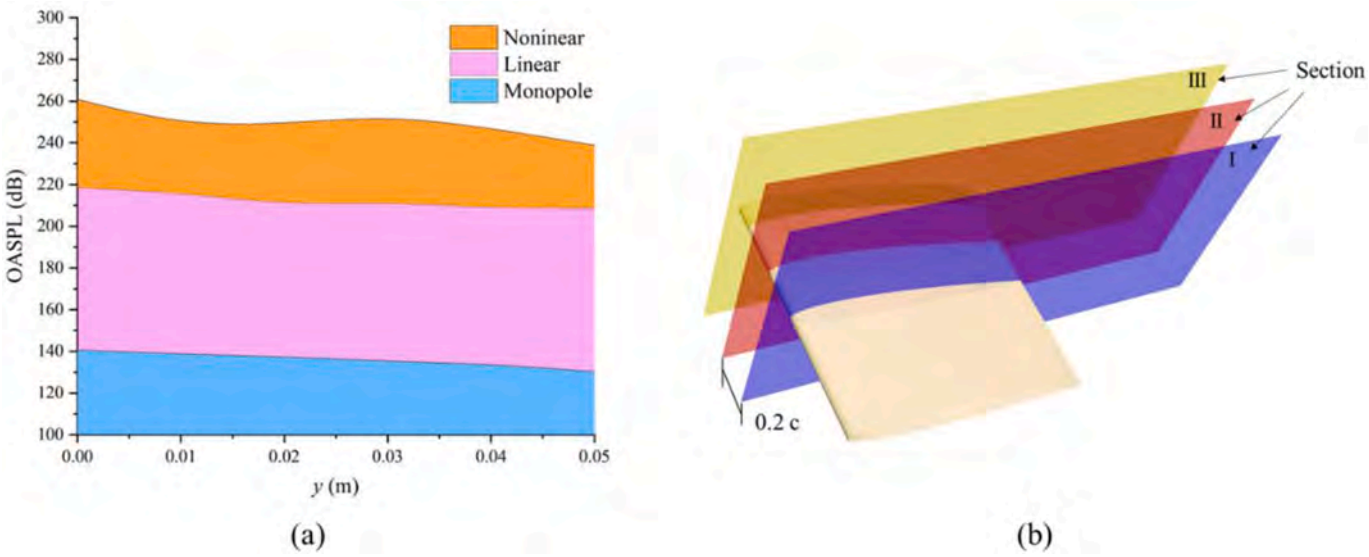

Fig. 20. (a) OASPL calculated for different components at 8 probes (B_1–B_8); (b) Three section planes in spanwise direction.

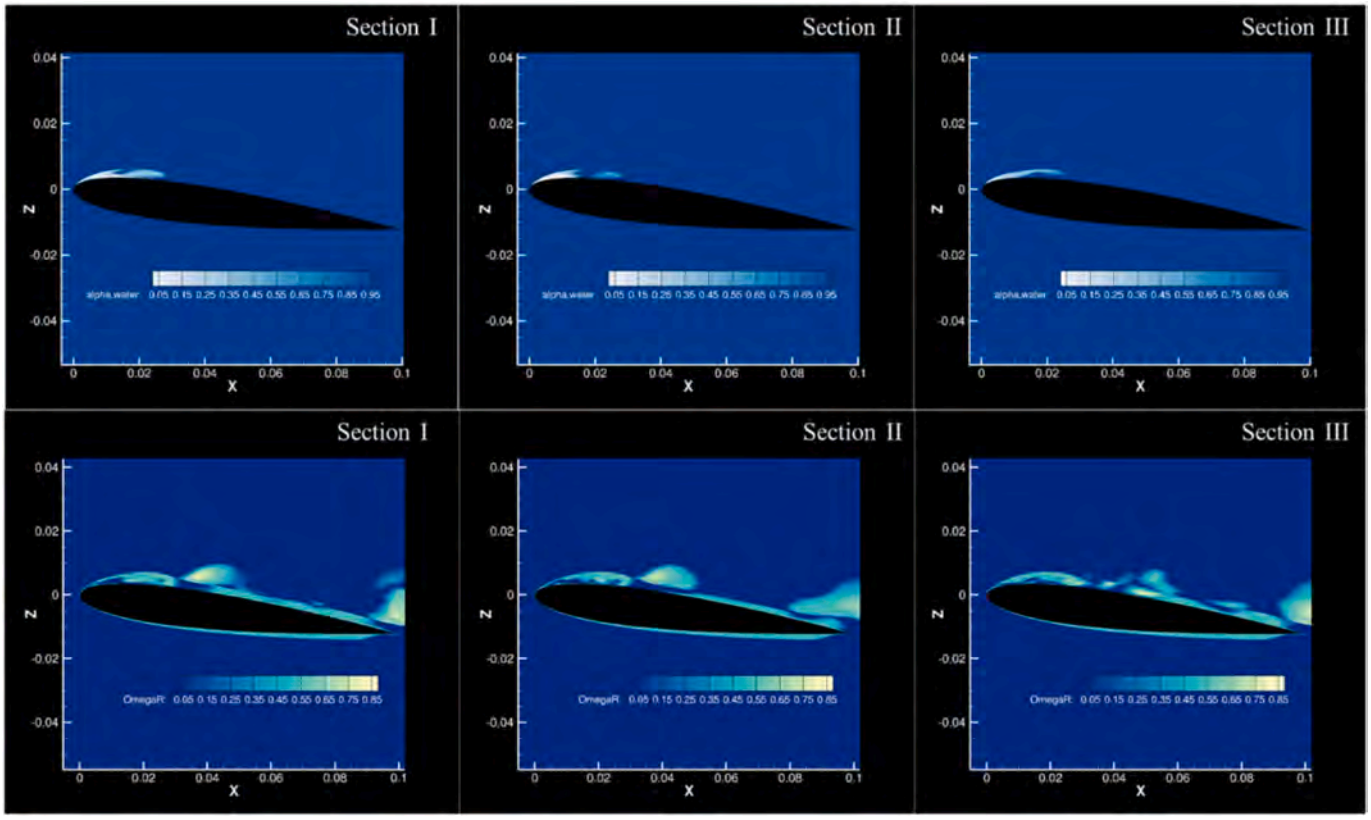

Fig. 21. The top panel: The cavitation maps in three sections; The bottom panel: $\boldsymbol{\Omega_R}$ cloud map in the third generation of vortex identification.

For underwater noise, the quadrupole plays an important role in the far field. Therefore, the nonlinear sound pressure of far field is predicted and compared with the literature results. 6 microphones are selected in the far field, denoted as 'A'-'F', whose coordinates are (50D, 0, 0), (100D, 0, 0), (50D, 50D, 0), (100D, 100D), (0, 50D, 0), (0, 100D, 0), as shown in Fig. 7. It can be seen that the results are in good agreement with the literature.

4. Numerical setup and experiment validation

Chapter 3 verifies the volume integration method, laying the foundation for the subsequent calculation of cavitation noise. Because the computation of cavitation noise is also based on volume integration (see section 2.3 and 2.4). The main purpose of chapter 4 and chapter 5 are to study the cavitation noise characteristics of hydrofoils. NACA0012 section is selected as the research object, whose experimental data are rich, especially for cavitation conditions.

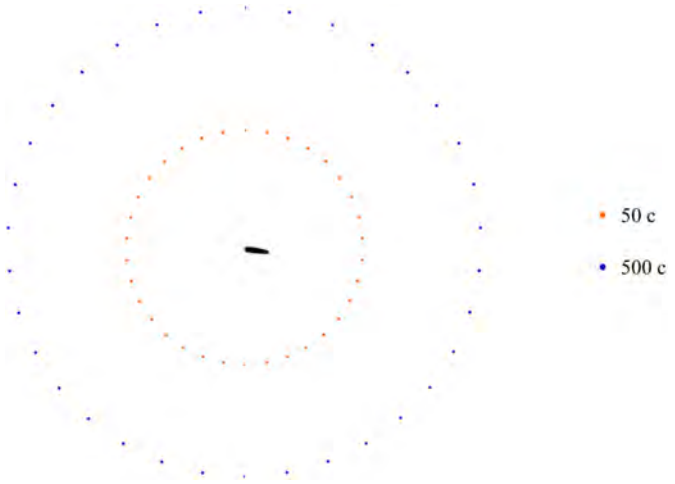

Fig. 22. The positions of far-field probes. The scale is partially distorted to show the effect.

4.1. Numerical computation setup

A 'C–H' type structure is adopted for the domain, as shown in Fig. 8. Structured grids are used to improve the mesh quality. The radius of the C-shaped structure is 2.0c, and the outlet patch is 4.0c length from the leading edge. Velocity inlet and pressure outlet boundary conditions are used for domain, and no-slip boundary conditions are adopted for other surfaces including the hydrofoil. The attack angle is marked as $\alpha = 7^{o}$. The number of grids is about 11.7 million.

Three acoustic volume integration ranges are set in this paper, represented by V_1, V_2, and V_3, respectively, as shown in Fig. 9. They contain the entire domain in the y direction, 0.5c in the z direction. and the lengths extends from the leading edge in the x direction by 2c, 2.5c, and 3c, respectively. All three ranges meet the MFP criteria for compact sound sources (Cianferra et al., 2019):

$$\mathrm{MFP} = \frac{1}{\Delta_{del} f_{max}} > 1 \tag{18}$$

where $\Delta_{del} = \frac{\max\limits_{y \in V} \left| y - x_{mic} \right| - \min\limits_{y \in V} \left| y - x_{mic} \right|}{c}$, c represents sound speed, V represents the volume for noise integration, x_{mic} is the microphone location, f_{max} is the max frequency of the fluid mechanics. When the MFP is greater than 1, the sound source is thought compact.

The third-generation vortex identification (Liu et al., 2019) is used in Fig. 9. It can be seen that V_3 contains almost all vortex cores.

4.2. Hydrodynamic validation

Three working conditions are set in this paper, the cavitation numbers are 2.85, 2.53, 2.27, respectively, and the angle of attack is 7deg. According to Ahn's experiment (Ahn et al., 2016), when $\sigma/2\alpha$

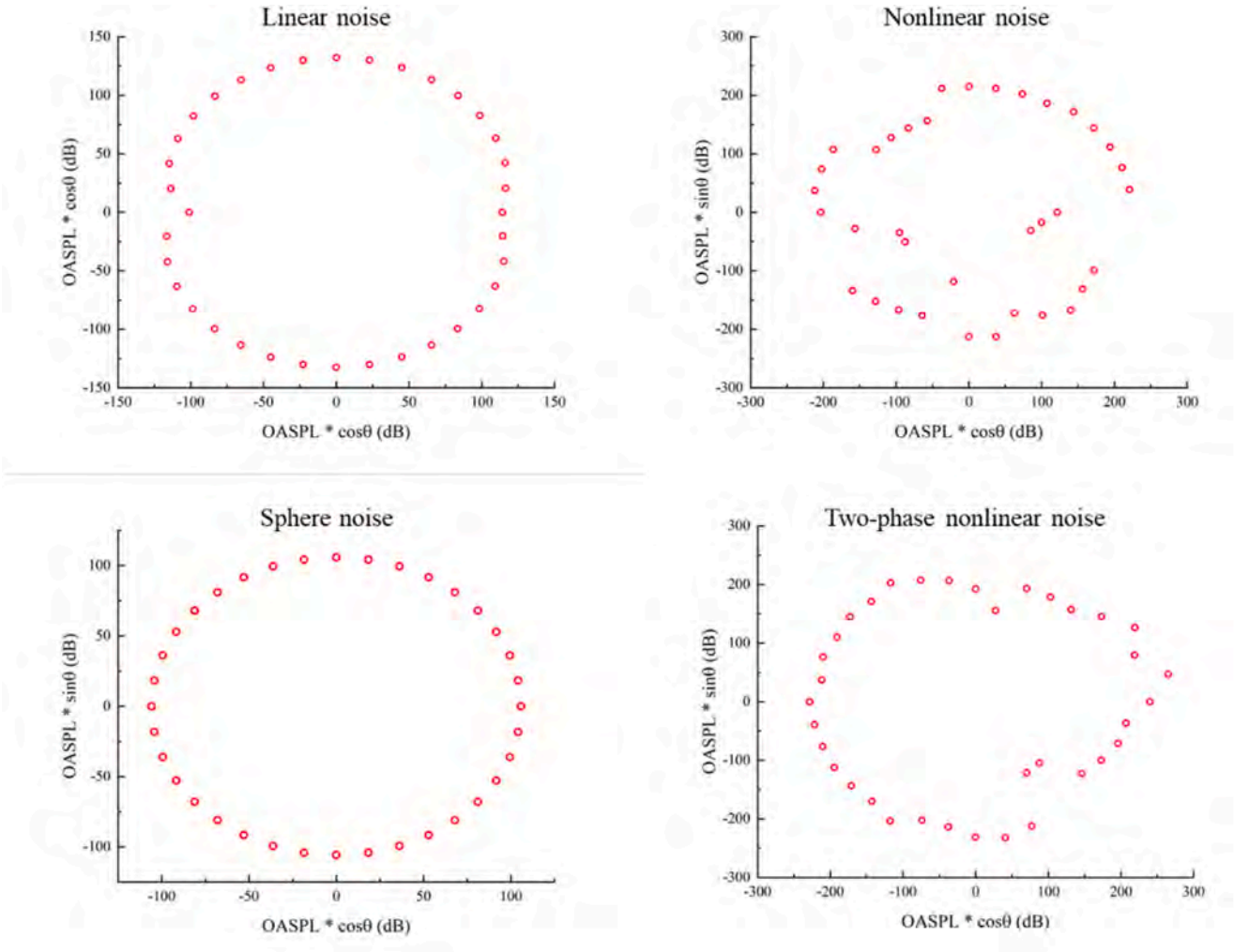

Fig. 23. The far-field acoustic directivity for 50c series.

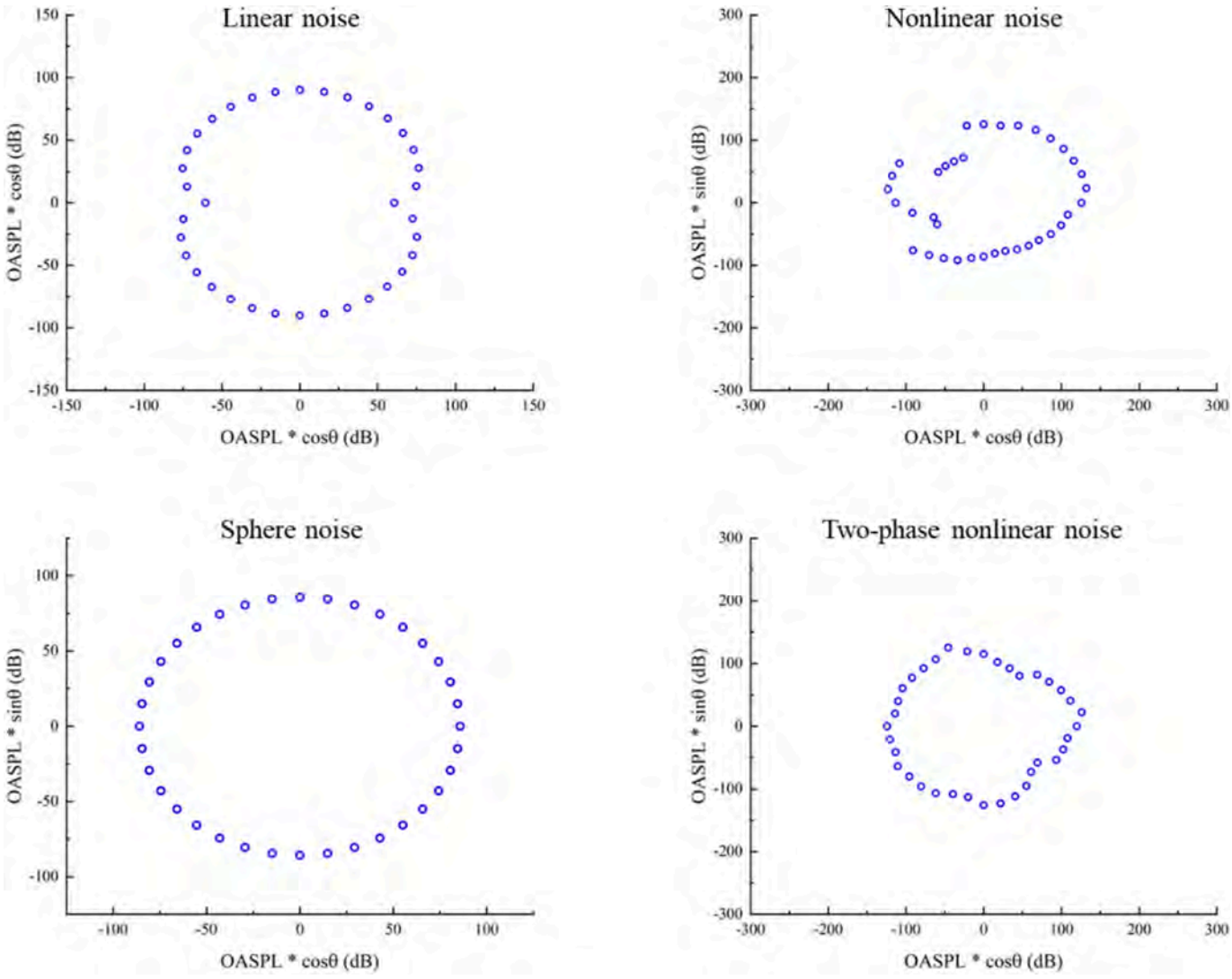

Fig. 24. The far-field acoustic directivity for 500c series.

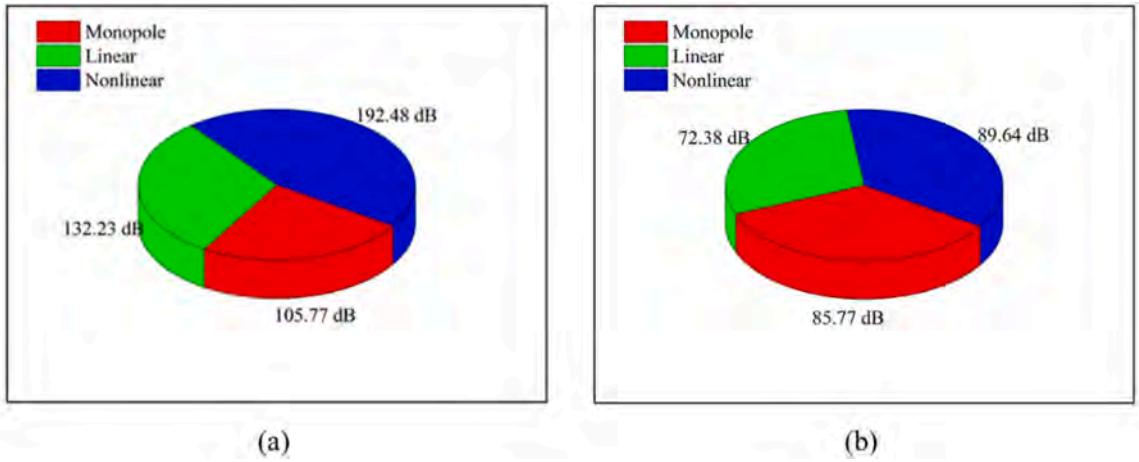

Fig. 25. Three components' relative size in the far field: (a) The 50c radius data; (b) The 500c radius data.

reaches a large value, the hydrofoil cavitation stays in sheet state. The three conditions in this paper belong to such state. Fig. 10 shows the simulated cavity shape compared with the experiment. The simulated cavitation length and the experiment results are shown in Table 1. The errors are within 5%.

Taking the $\sigma = 2.27$ as an example condition, the Strouhal number is obtained by the lift of the hydrofoil (the force in the positive z direction). The time-history result is transformed by FFT. As Fig. 11 shows, peak

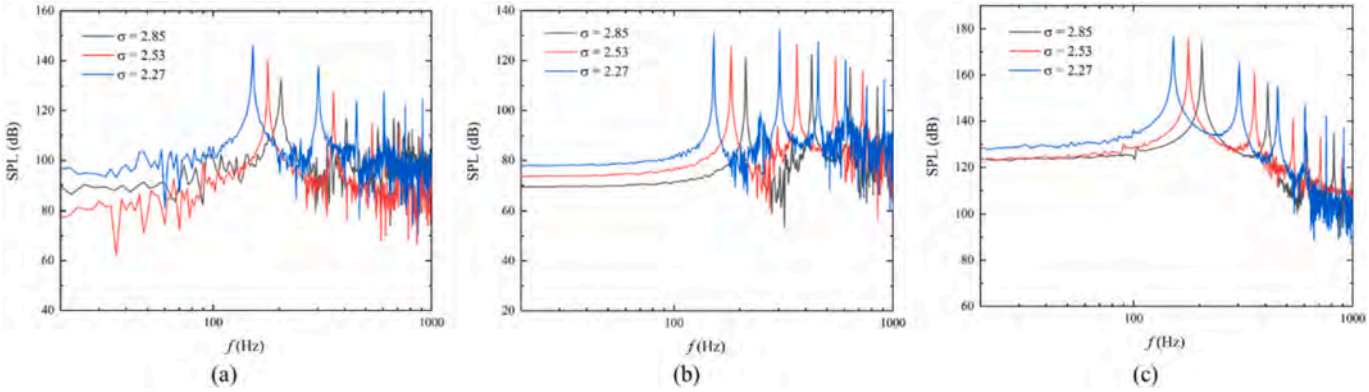

Fig. 26. Three components' results at A_4 and the black, red and blue lines represent $\boldsymbol{\sigma} = 2.85$, $\boldsymbol{\sigma} = 2.53$ and $\boldsymbol{\sigma} = 2.27$ respectively: (a) The linear component; (b) The sphere component; (c) The nonlinear component (computed by two-phase sound speed). (For interpretation of the references to color in this figure legend, the reader is referred to the Web version of this article.)

frequency is 150.2 Hz, and the corresponding St value is 0.395. Compared with the experimental result of 0.390, the error is 1.28%.

4.3. Acoustic validation

To verify the acoustic results, the same hydrophone as the experiment set is selected, as shown in Fig. 12. The $\sigma = 2.85$ condition is verified first, as Fig. 12 shows. It can be seen that the sound pressure value is significantly underestimated without considering the sound velocity variation.

Next, the results of the $\sigma = 2.53$ is compared in Fig. 13. Three acoustic integration ranges mentioned before are used. It is found that the results tend to converge. However, the error of V_3 is the smallest. Therefore, the following calculation and analysis are performed based on the V_3 integral.

We have known that ignoring sound velocity variations will underestimate the sound pressure. Under the working condition of $\sigma = 2.27$, we analyze the influence of different sound speed change methods on the results. The first two methods are step functions, and the thresholds are set $\alpha = 0.5$ and $\alpha = 0.9$ respectively. The last method is linear interpolation. Fig. 14 shows that step functions overestimate the sound pressure, and the effect of linear interpolation is significantly better than the first two ones. Therefore, linear interpolation method is taken to compute the sound speed.

5. Cavitation noise results and analysis

5.1. Streamwise acoustic characteristics

To study the acoustic streamwise distribution, 11 probes are arranged on the line ($z = 0.2$ c, $y = 0$), named as A_1, A_2, …, A_{11}. The microphones start at $x = 0$ (leading edge) with 0.1c intervals downstream, as shown in Fig. 15(a).

The linear noise component is integrated on the hydrofoil surface with Farrassat 1A formulation (Farassat, 2007). The nonlinear component is computed by the volume integration, and the range is V_3 introduced earlier. The spherical noise is also obtained by the volume integration of V_3. The spectrum of the normalized pressure fluctuation, S (f), is computed using FFT. For convenience, only four probes (A_1, A_4, A_7 and A_{10}) are plotted in each graph to illustrate the trend.

Observing the linear noise in Fig. 15(b), it can be found that the frequency characteristics of each microphone are similar. The first-order peak appears at about 150 Hz, followed by various higher-order peaks, and the values decrease gradually. Comparing the four test points, it is found that SPL at A_4 is higher than other probes, and the linear component decreases downstream gradually.

The first-order peak of nonlinear noise also appears on around 150Hz. Unlike the linear component, the maximum of nonlinear noise appears both at A_1 and A_4, as Fig. 15(c) presents. The low-frequency peaks arise as probe moves downstream (as the black box indicates), which is related to the development of turbulence and vortex shedding. The cavitating flow experiences four stages on the suction side sequentially: laminar, transition, turbulence and hairpin vortices. The low-frequency peaks downstream are believed associated with the hairpin vortex.

Compared with the other two components, sphere noise has more concentrated energy and more obvious peaks, as Fig. 15(d) displays. A maximum near the A_4 probe is shown, which can be explained from the sphere source. The cavitation ends near A_4, where the phase transfer appears drastically, and a concentrated area of sphere source arises.

The overall SPL (OASPL) of different components at 11 probes are plotted as area charts, as Fig. 16(b) shows. OASPL is calculated by:

$$E = \int S(f)df$$

$$OASPL = 10\log_{10}(E)$$

It can be seen that the nonlinear component has two peaks near A_0 and A_4, while the linear and sphere components both have one peak at A_4. In addition, both the linear and sphere components decrease downstream from A_4, but the nonlinear component has a second rise, which is related to the hairpin vortices of the hydrofoil, as Fig. 16(a) shows. Different from single-phase flow, the nonlinear component of cavitation noise is larger than the linear one in near fields. However, it is generally accepted that the near-field linear noise is higher than the nonlinear one for single-phase flow. Furthermore, the sphere component is smaller than the linear one in the near fields.

5.2. Spanwise acoustic characteristics

Similar to the streamwise distribution study, 8 probes are arranged spanwise. Since the peak of each component is located at x = 0.03m, the microphones are set on the line of z = 0.2c, x = 0.3c. Test points are evenly arranged from y = 0 to y = 0.4375c, which are recorded as B_1, B_2, …, B_8 in turn, as Fig. 17(a) shows.

The acoustic results of the linear, nonlinear and sphere components are plotted on one graph, as Fig. 17(b) shows. For convenience, only values of B_1 and B_8 are given here. It can be seen that the sound pressure in the middle part of hydrofoils is larger than that near the wall, and this conclusion is applicable to all three components. At the same time, all components show obvious peaks at around 150Hz.

As we all know, once cavitation occurs, it will dominate the noise. Therefore, the period of cavitation dominates the peak frequency of the sound pressure. The time history of cavity volumes is plotted and

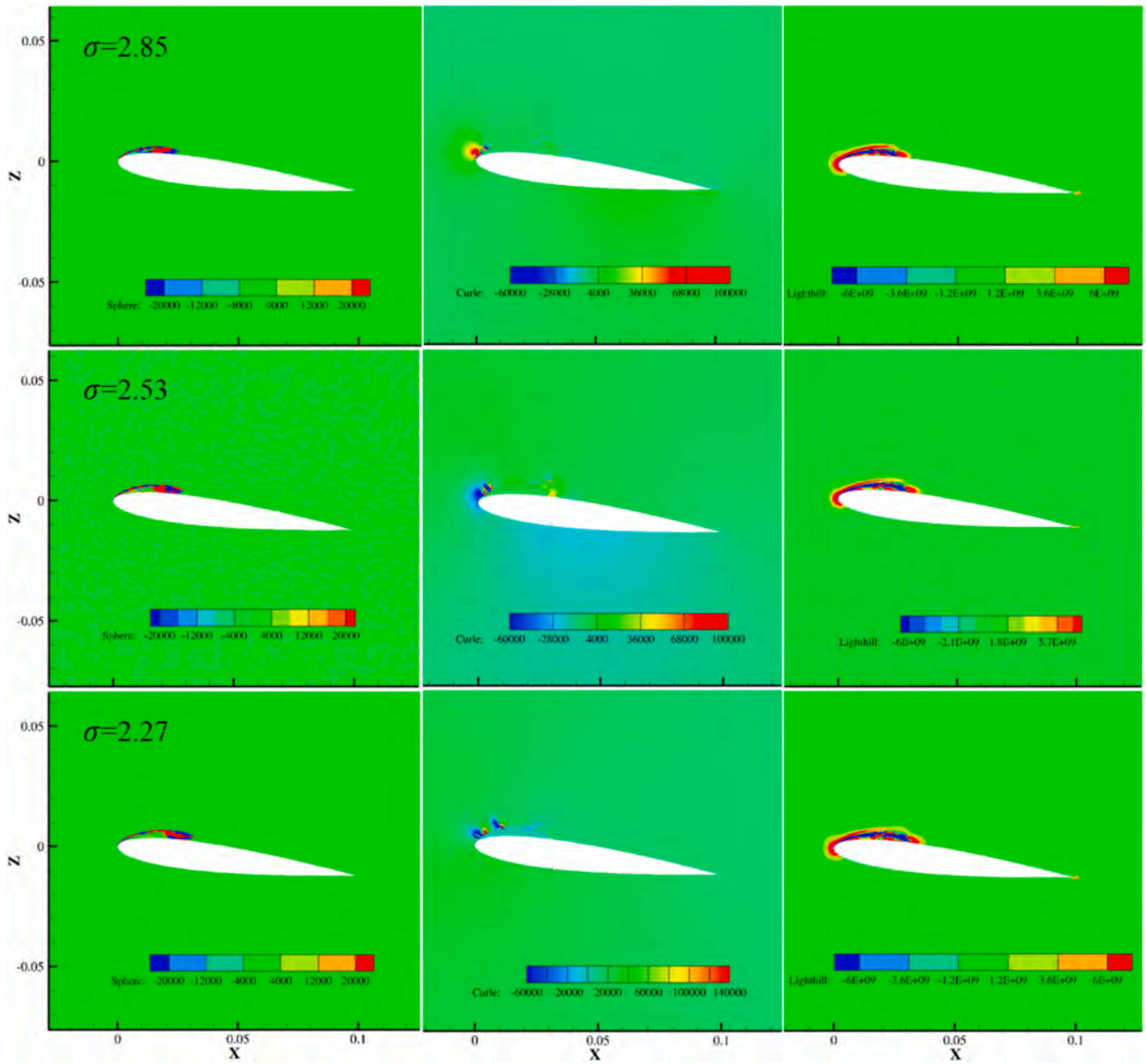

Fig. 27. The left panel: Sphere source ($\frac{\rho_0}{4\pi}\frac{\partial}{\partial t}\left[\frac{\partial \alpha_V}{\partial t}\right]$) distribution; The middle panel: Curle source ($\frac{1}{4\pi c}\frac{dp}{dt}$) distribution; The right panel: Lighthill source ($\frac{\partial^2(\rho v_i v_j)}{\partial x_i \partial x_j}$) distribution.

performed by FFT, as Fig. 18 shows. It is obvious that the frequency of the cavitation change is around 150Hz. Fig. 19 shows the typical stages of the hydrofoil sheet cavitation in a cycle, going through the development of the re-entrant jet and the growth of the sheet cavitation.

Similar to the streamwise study, the area chart of OASPL for the 8 probes is plotted spanwise, as Fig. 20(a) shows. It can be seen that the acoustic energy of all three components decrease from the middle to the wall. However, the nonlinear reduction is even greater. To explain such distribution, three sections are selected, from the middle to the wall in positive y direction, with an interval of 0.2c, numbered by Roman numerals I, II, and III in turn, as Fig. 20(b) shows.

From Fig. 21, it can be seen that the cavitation length decreases from section I to section III, which determines the strength of the sphere noise directly. For the vortex, from middle to the two sides, the vortex is broken gradually. Therefore, the nonlinear acoustic energy also decreases.

5.3. Far-field acoustic directivity

In order to investigate the far-field directivity, a series probes are set up on the y = 0 plane. Taking the leading edge as the center, 36 hydrophones are arranged every 10° with a radius of 50c and 500c respectively, as Fig. 22 shows.

Fig. 23 presents the result of 50c series probes. The linear directivity shows obvious dipole characteristics. As for the nonlinear directivity, two calculation methods are performed. One ignores the change of sound speed, and the other considers it. The amplitudes of the two approaches are similar. However, the front-to-rear ratio of lobes are obviously different. For the former method, the ratio seems too large, which may not be realistic.

For 500c series, the acoustic directivity is similar to 50c, see Fig. 24. However, it should be noted that compared to 50c, the spherical sound pressure drops slowly, while the nonlinear component drops quickly.

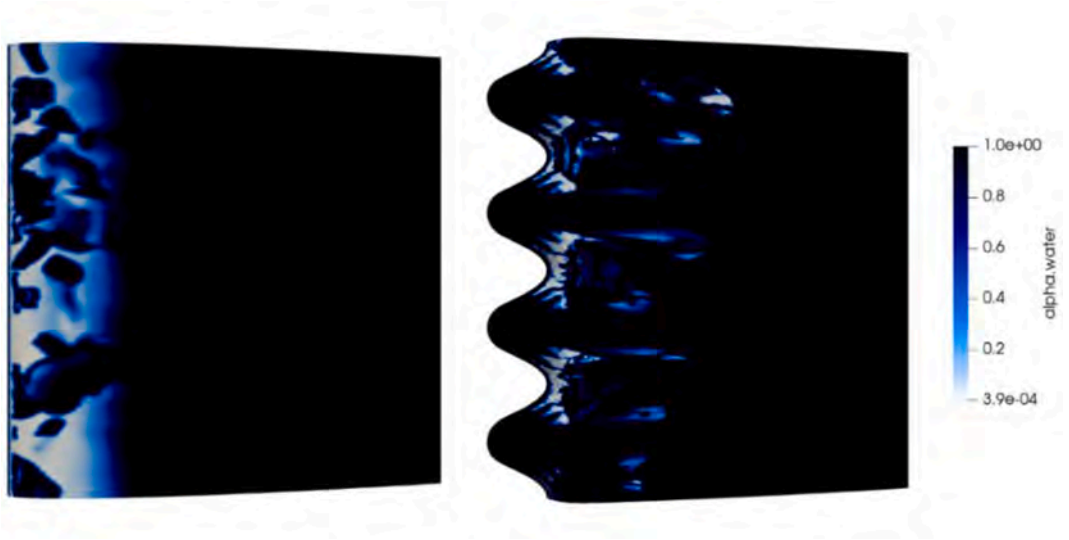

Fig. 28. The cavitation distribution on the suction surface: The left side is the baseline NACA0012 hydrofoil; The right side is the modified hydrofoil.

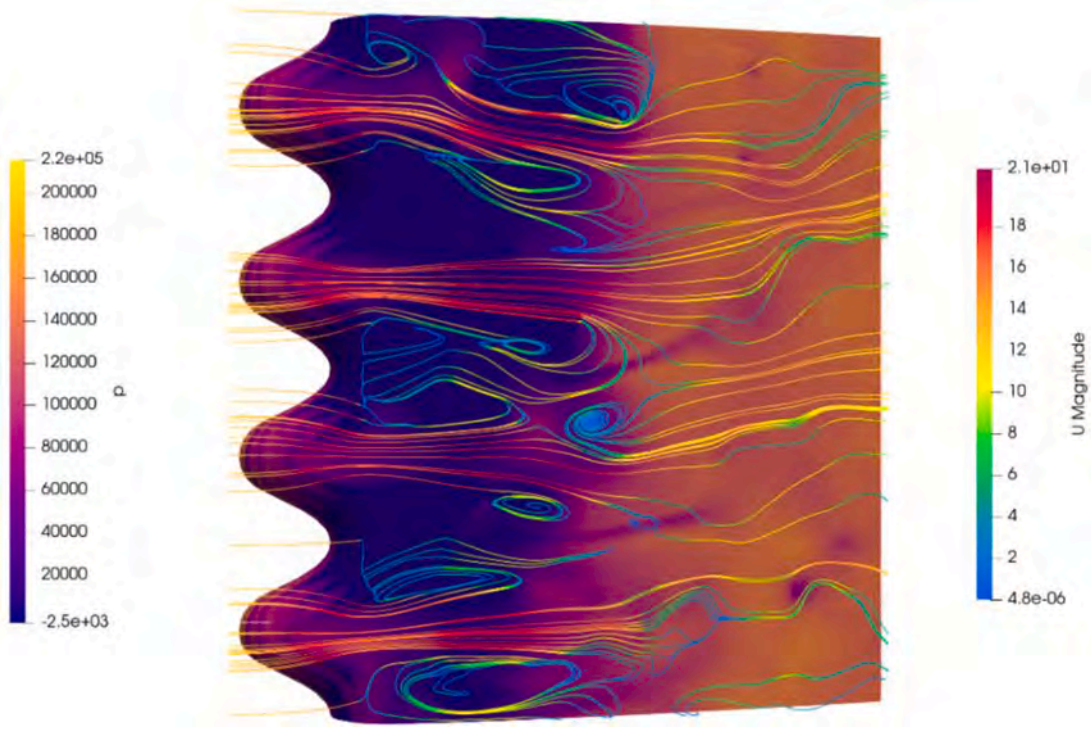

Fig. 29. The pressure distribution and streamlines on the suction surface. The streamlines are colored by velocity.

To compare the relative sizes of the components, a pie chart is drawn, see Fig. 25. Note that the total OASPL is not a direct sum of the decibel units of three components. It only expresses the magnitude relationship. For 50c radius, the nonlinear component is dominant absolutely, and the linear and spherical one follow in turn, see Fig. 25(a). At 500c distance, the nonlinear magnitude is already close to spherical OASPL, see Fig. 25 (b). It is foreseeable that, at further distances, the total sound pressure will be dominated by the sphere component.

5.4. *Effect of cavitation number*

The smaller the cavitation number, the more serious the cavitation phenomenon. The effect of cavitation number on hydrofoil noise is studied in this section. Working conditions are the previous ones with cavitation numbers 2.85, 2.53 and 2.27, respectively.

Fig. 26 shows SPL of three components at A_4. As the cavitation number increases, the peak frequency increases, and the amplitude decreases. Different components have various decreasing amplitudes: the linear pressure undergoes the most significant drop, and the sphere and nonlinear components have little decrease. This indicates that once cavitation occurs, the sphere and nonlinear acoustics are determined, and have little to do with the cavitation length.

Fig. 27 displays the sound source distribution of sphere noise, dipole noise and quadrupole noise with three cavitation numbers, and $y = 0$ slice is selected here. It can be seen that all sources are concentrated near the leading edge on the suction side, except for the quadrupole concentration in rear area. The magnitude of sphere, dipole and quadrupole source increase successively, consistent with the sound pressure

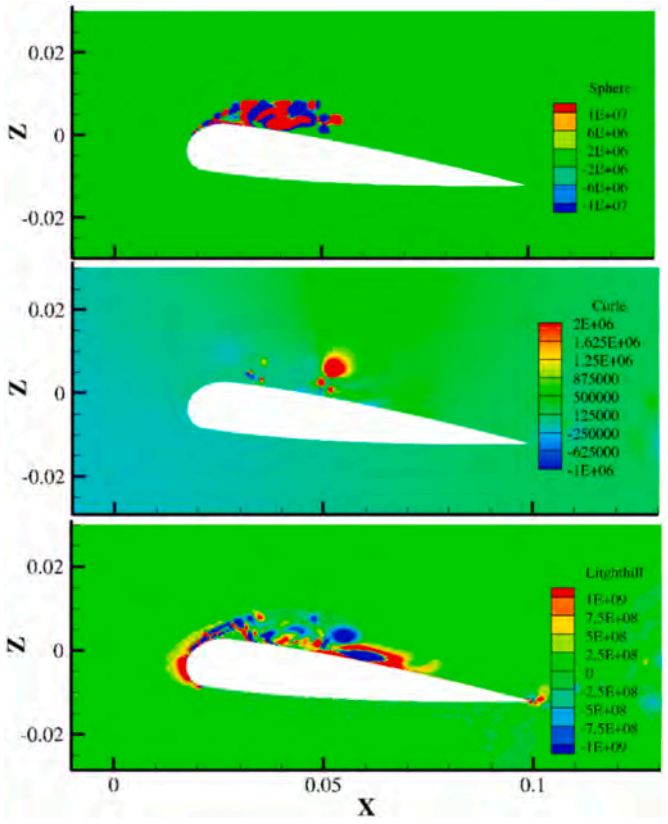

Fig. 30. The sound source distribution on the plane **y** = 0: The top panel is sphere source; The middle one is Curle source; The bottom is Lighthill source.

predictions in the near field.

The sphere source is centralized near the closure of the cavitation. As the cavitation number decreases, the cavity length increases. Therefore, the concentrated area of the sphere source moves downstream gradually. The difference is indistinct for the dipole distribution with the change of the cavitation numbers. The characteristics of the quadrupole is similar to that of the sphere source. As the cavitation number decreases, the range expands progressively. It should be noted that only the dipole on the hydrofoil surface is effective due to surface integration. For the convenience of comparison, the dipole distribution in the whole section is drawn here.

5.5. Modified hydrofoil cavitation noise

A number of bionic hydrofoils have been shown to improve the hydrodynamic properties. The purpose of this section is to investigate whether the modified hydrofoils' cavitation noise can be controlled, and to explore from the perspectives of sphere and nonlinear components. A wavy leading edge is selected in this paper and applied to NACA0012 hydrofoil. The parameters are the same as that mentioned in the literature (Li et al., 2020): the leading edge satisfies a sinusoidal curve (along y direction), the wavelength equals to 0.25c, and the amplitude is 0.12c. Other parameters are consistent with NACA0012 model. $\sigma = 0.227$ working condition is adopted in this section.

Fig. 28 displays the cavitation map on the hydrofoil suction side. It can be seen that the cavity is concentrated in the trough regions, while almost no cavitation occurs near the peaks. It can be explained from the pressure map. Fig. 29 shows the pressure distribution and streamlines on the suction side. Due to the geometry difference, the pressure near the peaks is smaller compared with that in trough area. Therefore, the incipient cavitation number increases at the trough regions, causing the cavitation earlier. Because of the spanwise pressure gradient between the troughs and peaks, the streamlines concentrate near the peaks. This affects the nonlinear sound pressure.

The sound source map of the modified hydrofoil is plotted, as shown in Fig. 30. The sound source distribution of the baseline hydrofoil is given in the third row of Fig. 27. To avoid repetition, the source distribution for NACA0012 is not redrawn. Compared with NACA0012, the magnitudes of two sources are increased by 1–2 orders. Among them, Curle source grows the most. The wavy leading edge changes the boundary layer flow, enlarging the pressure fluctuation on the hydrofoil surface. At the same time, it can be seen that the spatial ranges of the sphere and Lighthill source are extended significantly. The spherical source is related to the range of cavitation. The concave-convex leading edge enhances the cavitation, extending the distribution range of the sphere source. There is a strong interaction between cavitation and vortex. Therefore, the vortex shedding is also strengthened. As a result, Lighthill source lasts downstream long. However, Lighthill intensity becomes weakened.

Fig. 31 presents three components results at the A_4 position. Different from NACA0012, no obvious peaks of various orders are found for SPL of modified hydrofoil. There is a maximum value near 20Hz. The sound pressure decreases with the frequency. This is because the cavitation length of modified hydrofoil is longer. The type has changed from sheet cavitation to unsteady cavitation. The spanwise inhomogeneity also exacerbates such instability. Corresponding to the sound source diagram, linear and spherical sound pressure are both enhanced. However, nonlinear noise is significantly reduced. This is because the spanwise flow breaks vortex structures. Besides, for the modified hydrofoil,

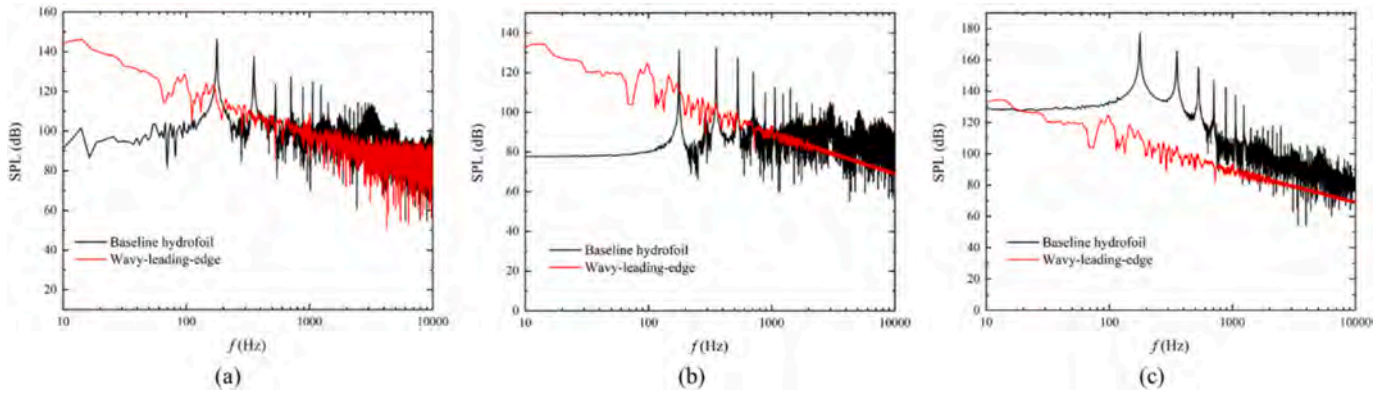

Fig. 31. Three components' results at A_3 and the black and red lines represent NACA0012 hydrofoil and leading-wavy-edge geometry respectively: (a) The linear component; (b) The sphere component; (c) The nonlinear component (computed by two-phase sound speed). (For interpretation of the references to color in this figure legend, the reader is referred to the Web version of this article.)

linear component is larger than spherical and nonlinear sound pressures. There is another reason why the source intensity of the bionic hydrofoil is stronger. As shown in Fig. 29, the streamline is pushed out, and the cavitation is more serious in rough regions. Fig. 30 shows the cut plane distribution at the groove. Therefore, the sound source enhancement is more obvious. More in-depth mechanisms for this noise distribution requires more systematic research and experiments in the future.

The frequency of sound heard by the general human ear is mainly concentrated in the range of 500–4000 Hz. In this frequency range, the sound pressure of the modified hydrofoil is lower. From the perspective of comfort, the wavy-leading hydrofoil has certain advantages. However, it has little effect considering the loss of hydrodynamic coefficient and processing cost. In author's opinion, it is not recommended to choose a bionic hydrofoil for civil use. However, the bionic hydrofoil can eliminate the peak signal characteristics obviously, which is helpful for equipment with high concealment requirements, such as military submarines, because it is difficult to be caught by sonar sacrificing part of the hydrodynamic performance. Therefore, it has certain potential in the military field.

6. Conclusion

In this paper, the direct volume integration of FW-H formulation is used to compute cavitation nonlinear noise, considering the sound velocity variation caused by the phase transitions. The sound pressure induced by the cavity volume change is represented by sphere noise. The cavitation noise of the NACA0012 hydrofoil and wavy-leading-edge modified hydrofoil are studied in detail. The focus is on the distribution characteristics of nonlinear sound pressure, spherical component, and linear noise. The conclusions are as follows:

(1) In the regard of the method accuracy, the sound value is underestimated ignoring the variation of sound speed. Compared with the step function, the sound velocity obtained by linear interpolation is closer to the experimental result.
(2) In terms of near-field characteristics, three noise components reach maximums near the cavity closure area. Different from single-phase URN, near-field nonlinear sound pressure is larger than the linear one for cavitation noise. Spherical component is the smallest. As for the spanwise distribution, noise decreases gradually from the middle to the sidewall for all three components. Peak frequency in the near field corresponds to the cavitation development period.
(3) In terms of far-field directivity, nonlinear OASPL exhibits quadrupole characteristics. Compared with that ignoring the sound speed variation, the front-to-back ratio of lobes is smaller for linear interpolation. The author believes that it is more realistic. As the distance increases, proportion of sphere noise increases. It seems to exceed the nonlinear noise and become dominant components eventually.
(4) For the influence of cavitation number, peak frequency declines as the cavitation number decreases, while the sound pressure value rises gradually. Distribution range of the sound source expands as cavitation number decreases. This proves that cavitation plays a dominant role for hydroacoustics.
(5) For the influence of geometry, the wavy-leading edge causes cavitation noise to rise, especially for spherical and linear components, although it shows advantages in hydrodynamics in single phase. The bionic geometry changes the streamline and pressure distribution, making cavitation and vortex shedding more intense, thus enhancing the noise.

Data availability

The data that support the findings of this study are available from the corresponding author upon reasonable request.

CRediT authorship contribution statement

Lianjie Yu: Data curation, Writing – original draft, preparation, Visualization, Investigation, Software, Validation. **Decheng Wan:** Supervision, Conceptualization, Methodology, Investigation, Writing – review & editing. **Jianwei Wu:** Software, Data curation, Visualization, Investigation, Validation.

Declaration of competing interest

The authors declare that they have no known competing financial interests or personal relationships that could have appeared to influence the work reported in this paper.

Data availability

Data will be made available on request.

Acknowledgements

This work was supported by the National Key Research and Development Program of China (2019YFB1704200), and the National Natural Science Foundation of China (51879159, 52131102), to which the authors are most grateful.

References

Ahn, B.K., Jeong, S.W., Kim, J.H., 2016. Experimental investigation of cavity patterns and noise characteristics. In: International Conference on Offshore Mechanics and Arctic Engineering, vol. 49989. American Society of Mechanical Engineers. V007T06A100.
Brentner, K.S., 1997. An efficient and robust method for predicting helicopter highspeed impulsive noise. J. Sound Vib. 203, 87–100.
Cianferra, M., Armenio, V., Ianniello, S., 2018. Hydroacoustic noise from different geometries. Int. J. Heat Fluid Flow 70, 348–362.
Cianferra, M., Ianniello, S., Armenio, V., 2019. Assessment of methodologies for the solution of the Ffowcs Williams and Hawkings equation using LES of incompressible single-phase flow around a finite-size square cylinder. J. Sound Vib. 453, 1–24.
Curle, N., 1955. The influence of solid boundaries upon aerodynamic sound, 1187. In: Proceedings of the Royal Society of London. Series A. Mathematical and Physical Sciences, 231, pp. 505–514.
Farassat, F., 2007. Derivation of Formulations 1 and 1A of Farassat. NASA Technical Report No. NASA/TM-2007-214853.
Ffowcs Williams, J.E., Hawkings, D.L., 1969. Sound generation by turbulence and surfaces in arbitrary motion. Phil. Trans. Roy. Soc. Lond. Math. Phys. Sci. 264 (1151), 321–342.
Greschner, B., Thiele, F., Jacob, M.C., Casalino, D., 2008. Prediction of sound generated by a rod–airfoil configuration using EASM DES and the generalised Lighthill/FW-H analogy. Comput. Fluid 37 (4), 402–413.
Ianniello, S., Muscari, R., Di Mascio, A., 2013. Ship underwater noise assessment by the acoustic analogy. Part I: nonlinear analysis of a marine propeller in a uniform flow. J. Mar. Sci. Technol. 18 (4), 547–570.
Ianniello, S., Muscari, R., Di Mascio, A., 2014. Ship underwater noise assessment by the Acoustic Analogy part II: hydroacoustic analysis of a ship scaled model. J. Mar. Sci. Technol. 19 (1), 52–74.
Kim, H.J., Durbin, P.A., 1988. Observations of the frequencies in a sphere wake and of drag increase by acoustic excitation. Phys. Fluid. 31 (11), 3260–3265.
Kim, S., Cheong, C., Park, W.G., 2018. Numerical investigation into effects of viscous flux vectors on hydrofoil cavitation flow and its radiated flow noise. Appl. Sci. 8 (2), 289.
Li, Z., Qian, Z., Ji, B., 2020. Transient cavitating flow structure and acoustic analysis of a hydrofoil with whalelike wavy leading edge. Appl. Math. Model. 85, 60–88.
Lighthill, M.J., 1952. On sound generated aerodynamically I. General theory, 1107. In: Proceedings of the Royal Society of London. Series A. Mathematical and Physical Sciences, 211, pp. 564–587.
Liu, C., Gao, Y.S., Dong, X.R., Wang, Y.Q., Liu, J.M., Zhang, Y.N., Gui, N., 2019. Third generation of vortex identification methods: omega and Liutex/Rortex based systems. J. Hydrodyn. 31 (2), 205–223.
Marine environment protection committee, 2014. In: IMO (Ed.), Noise from Commercial Shipping and its Adverse Impacts on Marine Life. MEPC 66/17.
Merkle, C.L., Feng, J.H., Buelow, P.E.O., 1998. Computational modeling of the dynamics of sheet cavitation. In: Proceedings of the 3rd International Symposium on Cavitation, Grenoble, France.
Moghadam, R.K., Javadi, K., Kiani, F., 2016. Assessment of the LES-WALE and zonal-DES turbulence models in simulation of the flow structures around the finite circular cylinder. J. Appl. Fluid Mech. 9 (2).
Pendar, M.R., Páscoa, J.C., Roohi, E., 2021. Cavitating flow structure and noise suppression analysis of a hydrofoil with wavy leading edges. In: 11th International Symposium on Cavitation. Daejon, Korea.

Schnerr, G.H., Sauer, J., 2001. Physical and numerical modeling of unsteady cavitation dynamics. In: Fourth International Conference on Multiphase Flow, vol. 1. ICMF New Orleans.
Seidl, V., Muzaferija, S., Perić, M., 1997. Parallel DNS with local grid refinement. Appl. Sci. Res. 59 (4), 379–394.
Seo, J.H., Lele, S., 2009. Numerical investigation of cloud cavitation and cavitation noise on a hydrofoil section. In: Proceedings of the 7th International Symposium on Cavitation. Michigan, USA.
Spalart, P.R., Allmaras, S.R., 1992. A one-equation turbulence model for aerodynamics flows. In: 30th Aerospace Sciences Meeting and Exhibit, p. 439.
Wei, A., Wang, S., Gao, X., Qiu, L., Yu, L., Zhang, X., 2022. Investigation of unsteady cryogenic cavitating flow and induced noise around a three-dimensional hydrofoil. Phys. Fluids 34 (4), 042120.
Wu, Q., Huang, B., Wang, G., Cao, S., Zhu, M., 2018. Numerical modelling of unsteady cavitation and induced noise around a marine propeller. Ocean Eng. 160, 143–155.
Zwart, P.J., Gerber, A.G., Belamri, T., 2004. A two-phase flow model for predicting cavitation dynamics. In: Multiphase Flow, Yokohama, Japan. Fifth International Conference on, vol. 152.